SOLID-STATE REFRIGERATION: A COMPARISON OF THE ENERGY PERFORMANCES OF CALORIC MATERIALS OPERATING IN AN ACTIVE CALORIC REGENERATOR

C. Aprea[1], A. Greco[2], A. Maiorino[1], C. Masselli[1*]

[1] *Department of Industrial Engineering, University of Salerno, Via Giovanni Paolo II 132, 84084, Fisciano (SA), Italy*

[2] *Department of Industrial Engineering, University of Naples Federico II, P.le Tecchio 80, 80125, Napoli, Italy*

*** Corresponding author: Tel. +39 089964002; Fax +39 089964037; e-mail: cmasselli@unisa.it**

Abstract

The energy performances of an Active Caloric Refrigerator are reported in this paper. An ACR is tested under a vast number of solid-state refrigerants exhibiting one of the four main caloric effects considered for refrigeration (magnetocaloric, electrocaloric, elastocaloric and barocaloric effect). The analysis is performed numerically through a 2D model, experimentally validated, that can reproduce the behavior of an Active Caloric Regenerator. Temperature span, cooling power and coefficient of performance are the indexes through which the comparison is carried out. The tests are performed at a fixed AMR cycle frequency (1.25 Hz), in the temperature range 292 – 300 K, varying the mass flux in the range 150 - 250 kg s^{-1} m^{-2}. The most promising caloric materials that have been tested as refrigerants are: Gd, $Gd_5Si_2Ge_2$, $LaFe_{11.384}Mn_{0.356}Si_{1.26}H_{1.52}$, $LaFe_{11.05}Co_{0.94}Si_{1.10}$ (magnetocaloric materials); P(VDF-TrFE-CFE)/BST polymer, 0.93PMN-0.07PT thin film, the $Pb_{1-3x/2}La_xZr_{0.85}Ti_{0.15}O_3$ with single and variable composition, $PbTiO_3$, $Pb_{0.8}Ba_{0.2}ZrO_3$, $Pb_{0.97}La_{0.02}(Zr_{0.75}Sn_{0.18}Ti_{0.07})O_3$(electrocaloric materials); $Cu_{68.13}Zn_{15.74}Al_{16.13}$, NiTi, $PbTiO_3$ (elastocaloric materials); $(NH_4)_2MoO_2F_4$, $MnCoGe_{0.99}In_{0.01}$ (barocaloric materials). Among them, PLZT and in particular $Pb_{0.97}La_{0.02}(Zr_{0.75}Sn_{0.18}Ti_{0.07})O_3$ show the best results, higher than every other caloric material tested, conferring to electrocaloric refrigeration globally the most promising behaviour.

Keywords: *Caloric refrigeration; Active Caloric Regenerator; caloric materials; magnetocaloric effect; elastocaloric effect; electrocaloric effect.*

NOMENCLATURE

Symbols

B	magnetic field induction, T
C	specific heat, J kg^{-1} K^{-1}
COP	coefficient of performance, -
E	electric field, V m^{-1}

G	mass flux, kg s^{-1} m^{-2}
H	magnetic field, A m^{-1}
k	thermal conductivity, W m^{-1} K^{-1}
L	length of the regenerator in fluid flow direction
M	magnetization, A m^{-1}
P	polarization, C m^{-2}
p	pressure, Pa
Q	power density associated to caloric effect, W m^{-3}
$\dot{Q}$	power, W
RCP(S)	entropy relative cooling power, J kg^{-1}
RCP(T)	temperature relative cooling power, K^2
S	entropy, J $K^{-1}m^{-3}$
T	temperature, K
t	time, s
u	longitudinal fluid velocity, m s^{-1}
V	volume, m^3
v	orthogonal fluid velocity, m s^{-1}
$\dot{W}$	mechanical power, W
X	conjugate field
x	longitudinal spatial coordinate, m
Y	applied driving field
y	orthogonal spatial coordinate, m

Greek symbols

Δ	finite difference
δ	infinitesimal difference
ε	strain
$\bar{\varepsilon}$	infinitesimal quantity

η	efficiency, -
θ	period of ACR cycle, s
ν	cinematic viscosity, $m^2\ s^{-1}$
ρ	density, $kg\ m^{-3}$
σ	stress, Pa
τ	period of each step of ACR cycle, s

Subscripts

$_0$	minimum
$_1$	maximum
$_{ad}$	adiabatic
$_C$	cold heat exchanger
$_{CF}$	cold-to-hot flow process
$_{FWHM}$	full width at half maximum
$_f$	fluid
$_{FD}$	field decreasing
$_{FI}$	field increasing
$_H$	hot heat exchanger
$_{HF}$	hot-to-cold flow process
$_{MAX}$	at maximum
$_p$	pump
$_{ref}$	cooling
$_{rej}$	heat rejected
$_s$	solid
$_{span}$	span across ACR cold and hot side

1. Introduction

The world in which we live today is characterized by deep environmental disasters and increasing pollution that results in global warming and sudden climate changes. Today we are the tenants of the world that tomorrow will be inhabited by our progenies. The point is that today we are not able to guarantee them an environmentally friendly future if we do not begin to drastically change the way we live, produce and consume. Demand of energy is growing continuously and more than 20% of energy consumption is due to refrigeration and air conditioning. Even if, over the last two decades, many efforts have already been made to reduce energy consumption, we are still far from acceptable threshold values. Among the many reasons of such data there is also, in some sectors, the still being linked to yesterday's technologies due to the absence of adequate substitutes. As a matter of fact, vapor compression has ruled the market extensively for many years. It is still the predominant technique [1] among industrialized and commercialized refrigerators and HVAC systems, even if it has provoked ozone depletion crisis, due to employment of CFC and HCFC refrigerants whom have been forbidden by Montreal Protocol [2] and substituted by HFCs. HFCs, in turn, have given a big boost to global warming and climate change so that they have been progressively phased out by the Kyoto Protocol [3] and substitutes by other classes of refrigerants (natural fluids, hydrofluoroolefins…) [4]. A more drastic step would be the progressive banning of the vapor compression itself if it could be replaced by a strong alternative. With this in mind, the scientific community has devoted huge efforts in developing possible alternative cooling techniques that would be ecological, performing and characterized by low energy consumptions. Among these alternatives, there is caloric refrigeration [5] that belongs to the solid-state class of cooling techniques also known as non-vapor compression technologies, or not-in-kind (NIK) cooling technologies. They have gained remarkable attention [6] since, taking vapor compression as reference, caloric refrigeration holds a potential for: improvements in energy efficiency; reduction of environmental impact since it employs solid-state materials with no direct Ozone Depletion Potential (ODP) and zero direct Global Warming Potential (GWP); reliability and manageability since it is characterized by more compact systems and acoustic comfort due to lower noise levels.

Caloric refrigeration embraces other four main cooling techniques, each one based on a different caloric effect; such physical phenomena are exploited in a growing number of numerical and experimental cooling applications [7]. As a matter of fact, these techniques are linked to the group of materials that show a magnetocaloric, electrocaloric, elastocaloric and barocaloric effect, phenomena where the variation in the temperature of caloric material is registered when an applied external field changes in adiabatic conditions.

Magnetic refrigeration, based on magnetocaloric materials exhibiting a caloric effect under a variation of an external magnetic field, has been the pioneer of caloric cooling since it has been well-studied and investigated for room temperature application over the past thirty years. In truth, the interest in magnetic refrigeration began with the discovery of the magnetocaloric effect attributed to Weiss and Piccard [8] in 1917 but the turning point is located in 1982 when Barclay introduced [9] the use of reciprocating thermal regenerators (Active Magnetic Regenerators) coupled to a thermodynamic cycle, giving rise to a regenerative magnetocaloric cycle called Active Magnetic Regenerative (AMR) refrigeration cycle. The AMR cycle proved to be essential to achieve higher temperature span. The AMR cycle uses MagnetoCaloric Material (MCM) itself as both a refrigerant and regenerator such that the heat transfer process and regeneration process are coupled into a single process. The MCM is heated by magnetization and is cooled by demagnetization. In the last three decades a number of prototypes of magnetocaloric refrigerators has been developed. Most of them is founded on AMR cycle [10-15] classified basing: on rotative or alternative design; else on the nature of magnetic field generator (permanent magnets, superconducting magnets, electromagnets). In 2010, Kitanovski proposed [16] the concept of solid-state magnetic refrigerator founded on the Peltier effect that served as the thermal diode in order to manipulate and control the heat transfer direction. Even if the idea is promising, there are some disadvantages to be accounted like thermal resistance, electric resistance, durability and cost of the Peltier element. Recent studies have identified weaknesses [17,18] points of magnetic refrigeration and tried to improve them [19, 20]: as a matter of fact, most of the criticism lays in the high costs in magnetic field generating and the expansiveness of the most promising magnetocaloric refrigerants [21].

Electrocaloric Refrigeration (ER), which found is working principle on ElectroCaloric Effect (ECE), grew in a more recent past [22]. ECE is detected in ferroelectric materials (ElectroCaloric Materials, ECMs) showing an adiabatic temperature change while an applied electric field varies its intensity. Dually to magnetic refrigeration, the reference cycle for such technique is Active Electrocaloric Regenerative (AER) refrigeration cycle. The easy and relatively cheap electric field generation, together with the flexibility in producing high electric fields in large volumes, are the strong points of electrocaloric refrigeration. ER allows theoretically to reach values around 50 % of Carnot COP in small-scale applications [23]. A number of promising electrocaloric materials has been developed and most of them has a significant electrocaloric effect in a wider temperature range if compared with magnetocaloric materials [24,25]. Moreover, electrocaloric refrigerants belong mostly to ceramics and polymers, materials with relatively low costs. The number of developed prototypes of electrocaloric refrigerators [26,27] is really exiguous; huge disadvantages are related to the difficulties in electrically insulating the regenerators to prevent the occurrence of Eddy currents during the fluid flowing.

By stretching or pressing adiabatically the working materials with elastic properties, elastoCaloric Effect (eCE) or BaroCaloric Effect (BCE) occur. Such phenomena are the fundamental of elastocaloric [28] and barocaloric refrigerations [29], two early caloric cooling techniques emerging in the latest past. Active reverse Brayton based thermodynamic cycles are still the most practical and easy-applying also for eCE and BCE giving rise to cooling or heat pump cycles. Elastocaloric cooling employs mostly shape memory alloys (elastoCaloric Materials, eCMs). Even if a huge number of eCMs and BaroCaloric Materials (BCMs) are ongoing to be developed [30-33] by all-over the world scientists and research-groups, there are no barocaloric prototypes, whereas the account of the developed elastocaloric one is really small and they are early status at all: there are three elastocaloric based heat-pumps [34-36] developed in 2016-2017 biennium; in 2017 Engelbrecht et al. published [37] initial experimental results of a regenerative elastocaloric device and lastly Kirsch et al. [38] introduced an air conditioning system based on shape-memory alloys.

As a matter of fact, a key point that strongly influences the energy performance of a caloric prototype is the choice of the caloric solid-state refrigerant which best suits the application. Most of the time the novel developed materials are, firstly, tested numerically by means of models. The inherent state of the art contains a number of models of AMR regenerator [39-43], whereas very few are the models that test the energy performances of electrocaloric [44-46] and elastocaloric [47-50] materials and, furthermore, there are no barocaloric models in literature. To provide a general framework, we have developed a two-dimensional model of an Active Caloric Refrigerator (ACR) which can support any caloric solid-state material, regardless of the particular caloric effect. In the investigation introduced in this paper, the ACR has been tested with many solid-state materials exhibiting the four main caloric effects (MCE, ECE, eCE, BCE) and the relative energy performances have been carried out.

2. Caloric effect and active caloric regenerative refrigeration cycle

Caloric refrigeration is based on the same working principles, both as regard the physical of the caloric phenomenon at the base, and as regard the active thermodynamic cycle. Therefore, in this section, such concepts are treated generalizing. Caloric effect manifest itself in caloric materials, as reversible thermal changes, due to a variable driving field, which can be shown as entropy or temperature change, depending on whether the process is isothermal or adiabatic, respectively:

$$\Delta s = \int_{Y_0}^{Y_1} \left(\frac{\partial X}{\partial T}\right)_Y dY \tag{1}$$

$$\Delta T_{ad} = -\int_{Y_0}^{Y_1} \frac{T}{C} \left(\frac{\partial X}{\partial T}\right)_Y dY \tag{2}$$

Y and X represent the generic applied and conjugate field, respectively. In table 1 are reported the correspondence between Y and X and the particularized caloric effects. In correspondence of a magnitude growing of the driving field $\Delta s<0$ and $\Delta T_{ad}>0$ if the caloric effect is direct; dually $\Delta s>0$ and $\Delta T_{ad}<0$ are associated to inverse effect.

Caloric effect	**X**	**Y**
Magnetocaloric	M	H
Electrocaloric	P	E
Elastocaloric	ε	σ
Barocaloric	v	P

Table 1. Correspondence among generical and particularized caloric effects.

As predicted before, the active caloric thermodynamic cycles of the four above mentioned caloric techniques can be generalized in an Active Caloric Regenerative refrigeration (ACR) cycle which is Brayton-based and it is composed of four steps.

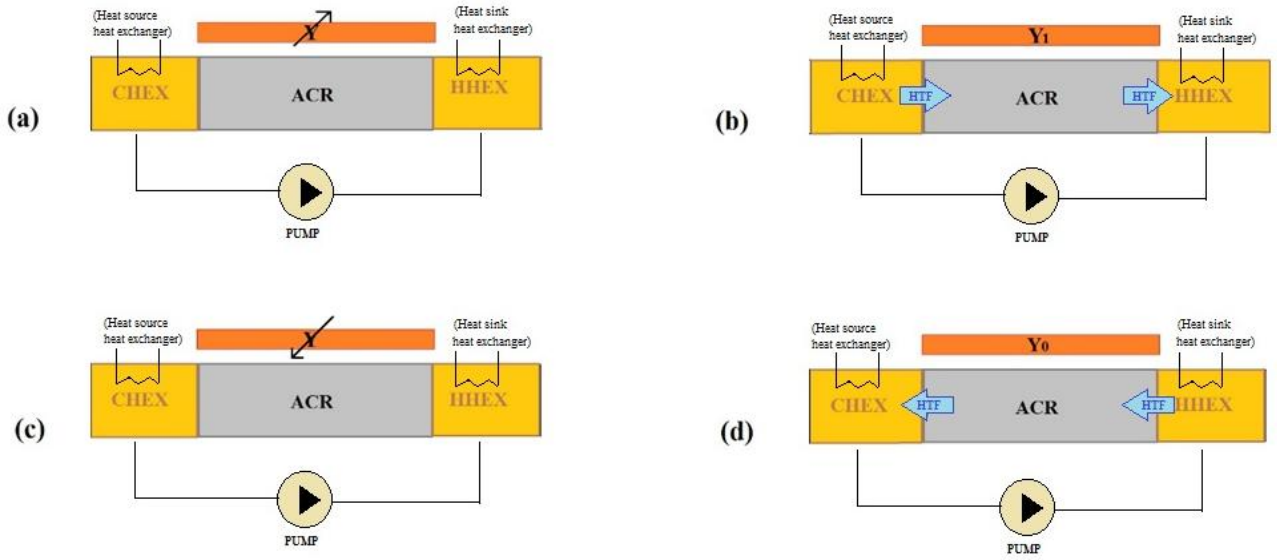

Figure 1. The four steps of Active Caloric Regenerative refrigeration cycle: a) adiabatic field-growing; b) CHEX to HHEX flowing; c) adiabatic field-falling; d) HHEX to CHEX flowing.

With reference to Figure 1, considering an ACR located among a Cold Heat EXchanger (CHEX) and a Hot Heat EXchanger (HHEX), in the first step (a) the applied driving field is growing, adiabatically, from a minimum (Y_0) to a maximum (Y_1) (Figure 1a). Therefore, by magnetization, polarization, stretching or pressing, the regenerator, made up of caloric material, grows its temperature by means of MCE, ECE, eCE or BCE. Then, as visible in Figure 1 (b), by means of a pump (or a piston), the heat transfer fluid cools the ACR, crossing it, from CHEX to HHEX, where, in the latter, it rejects heat. The third step (c) is characterized by adiabatic field decreasing from Y_1 to Y_0 while the Heat Transfer Fluid (HTF) does not move, so a further temperature reduction in ACR is registered, thanks to caloric effect. The last step (d) sees HTF passing through the regenerator by means of a pump (or a piston): as a result, HTF cools down and goes into CHEX where it subtracts heat, giving rise to the useful effect of the cycle.

3. A two-dimensional model of an Active Caloric Regenerator

The investigation introduced in this paper has been performed by means of a developed two-dimensional model of a caloric refrigerator. The model can reproduce the behavior of an Active Caloric refrigerator operating at room temperature, whatever is the caloric effect considered (MCE, ECE, eCE, BCE…), in a wide range of operating conditions, such as cold and hot reservoir temperature, mass flux, intensity of field variation, ACR working frequency. Geometrically the model constitutes of a two-dimensional parallel-plate regenerator; among the caloric plates HTF flows interstitially. The regenerator is located between CHEX and HHEX, whose presence is counted by proper boundary conditions.

3.1 Regenerator design

Figure 2 shows the design of the regenerator: a white stack of plates bounded by an H x L packaging (20 x 45 mm^2) forms the caloric solid-state refrigerant; whereas yellow are the channels for fluid crossing. Each solid-state plate is 0.25mm thick; the distance between two plates is 0.125 mm and it corresponds to the thickness of a single channel. Dually the distance between two channels is 0.25 mm.

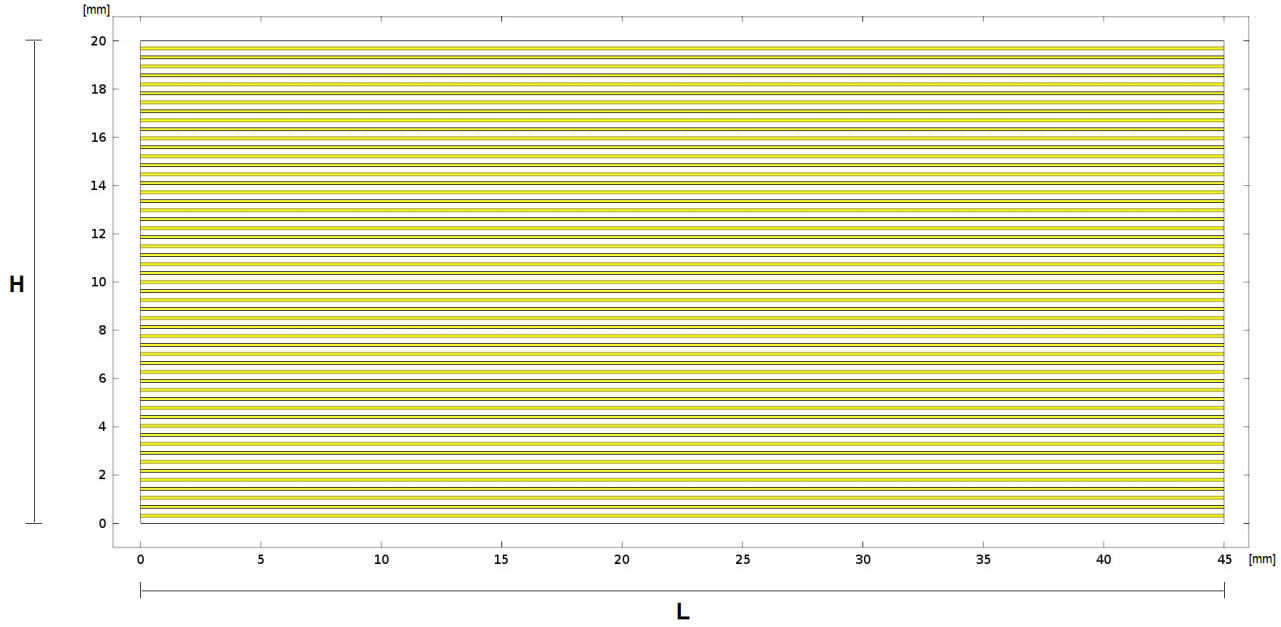

Figure 2. Design of the caloric regenerator.

3.2 Mathematical model

The regenerator described in section 3.1 is the domain where different sets of equations are applied, in correspondence of the current ACR process. As a matter of fact, the regenerator is subjected to the four processes of the ACR cycle, repeated cyclically. During the processes of fluid crossing, the regenerator is governed by energy (both for fluid and solid) and Navier-Stokes equations as follows:

$$\begin{cases} \dfrac{\partial u}{\partial x}+\dfrac{\partial v}{\partial y}=0 \\ \dfrac{\partial u}{\partial t}+u\dfrac{\partial u}{\partial x}+v\dfrac{\partial u}{\partial y}=-\dfrac{1}{\rho_f}\dfrac{\partial p}{\partial x}+\upsilon\left(\dfrac{\partial^2 u}{\partial x^2}+\dfrac{\partial^2 u}{\partial y^2}\right) \\ \dfrac{\partial v}{\partial t}+u\dfrac{\partial v}{\partial x}+v\dfrac{\partial v}{\partial y}=-\dfrac{1}{\rho_f}\dfrac{\partial p}{\partial y}+\upsilon\left(\dfrac{\partial^2 v}{\partial x^2}+\dfrac{\partial^2 v}{\partial y^2}\right) \\ \dfrac{\partial T_f}{\partial t}+u\dfrac{\partial T_f}{\partial x}+v\dfrac{\partial T_f}{\partial y}=\dfrac{k_f}{\rho_f c_f}\left(\dfrac{\partial^2 T_f}{\partial x^2}+\dfrac{\partial^2 T_f}{\partial y^2}\right) \\ \dfrac{\partial T_s}{\partial t}=\dfrac{k_s}{\rho_s c_s}\left(\dfrac{\partial^2 T_s}{\partial x^2}+\dfrac{\partial^2 T_s}{\partial y^2}\right) \end{cases} \quad (3)$$

The assumptions made are to operate with a laminar and incompressible fluid and to neglect the viscous dissipation since the mass flow is small. To model opportunely the fluid direction, the velocity vector has been considered positive if fluid flows from CHEX to HHEX, negative otherwise. During the fluid flow process, the interaction among the regenerator and the cold and hot heat exchangers is entrusted to Dirichlet boundary conditions: in the cold-to-hot flow process the CHEX mean temperature T_C is imposed in the left side; in the hot-to-cold T_H (HHEX mean temperature) is forced on the right side.

During the adiabatic field-changing steps the fluid is still, and the model is ruled by the energy equations for fluid and solid-state materials as follows:

$$\begin{cases} \rho_f C_f \frac{\partial T_f}{\partial t} = k_f \left(\frac{\partial^2 T_f}{\partial x^2} + \frac{\partial^2 T_f}{\partial y^2} \right) \\ \rho_s C \frac{\partial T_s}{\partial t} = k_s \left(\frac{\partial^2 T_s}{\partial x^2} + \frac{\partial^2 T_s}{\partial y^2} \right) + Q \end{cases} \tag{4}$$

The coupled boundary condition in this process is thermal insulation applied to all the boundaries.

The consequent caloric effect is taken in count in the solid by means of Q:

$$Q = Q(field, T_S) = \frac{\rho_s \, C \, (field, T_s) \Delta T_{ad}(field \, , T_s)}{\tau} \tag{5}$$

Q is a power density constructed to be proportional to $\Delta T_{ad}(field \, , T_s)$ and, therefore Q is a function of the intensity of the applied field. Q is positive during adiabatic field-growing, negative during adiabatic field-decreasing. This solution makes the model adaptable for every type of caloric effect and consequentially the model can reply the behavior of every Active Caloric Regenerative refrigeration cycle. As a matter of fact, Q is a further mathematical expression obtained by elaboration and manipulation of experimental data of C(field, T_S) and $\Delta T_{ad}(field \, , T_s)$, available from scientific literature, by the help of a mathematical finder software. A detailed description of Q construction is provided in section 4.

3.3 Model solving

The model is solved by means of Finite Element Method: through a meshing, the regenerator is divided into a set of smaller and shape-simpler mini-domains, called finite elements. Every element experiences its own ACR cycle and the results are then assembled into a larger system (the regenerator) that replies the entire problem. Figure 3 reports a zoom of the regenerator meshing: an unstructured triangular meshing has been built. Triangular mesh is a quick and easy solution for most of the domain and easily adaptable for rectangular structure. In the domain triangles are smaller where a greater accuracy is required (higher gradients).

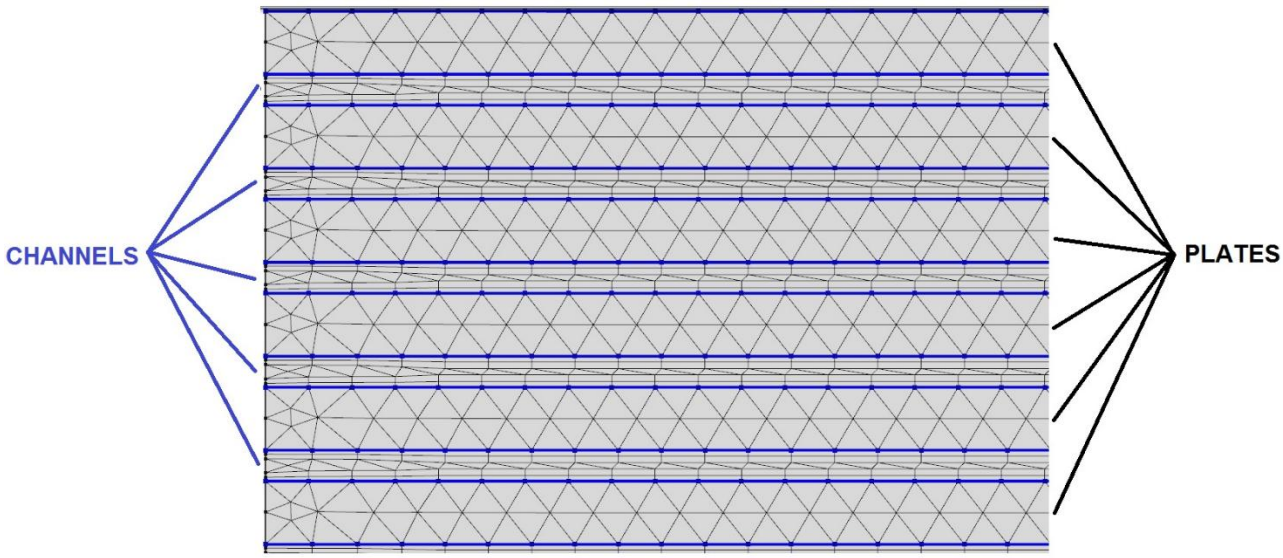

Figure 3. A focus on regenerator triangular mesh built for solving the model.

ACR cycles are applied to the regenerator as repeated sequences of four time-dependent sequential steps until reaching steady-state. For this purpose, the initial condition of each thermodynamic step is the last condition of the previous one, so that a time-based sequential condition can be applied. The period of each step of ACR cycle is τ (the same for all the ACR steps), whereas the period of each ACR cycle is θ and, therefore,

$$\theta = 4\tau \tag{6}$$

The ACR cycle is repeated n times until the regenerator reaches steady-state operation. Steady-state operation, ideally, takes place when in every point of the ACR regenerator the temperature at the beginning and at the end of the cycle is the same:

$$T(x, y, 0 + n\theta) = T(x, y, 4\tau + n\theta) \tag{7}$$

Therefore, to ensure the achievement of such condition, the cyclicality criterion must be satisfied in the ACR regenerator:

$$\delta = max\{T(x, y, 0 + n\theta) - T(x, y, 4\tau + n\theta)\} < \bar{\varepsilon} \tag{8}$$

4. Caloric materials

The choice of the caloric solid-state refrigerant to be used in relation to the working temperature range and the applications to which it is addressed, must take into account several variables. As a matter of fact, alongside the specific ones related to each particular caloric effect, it is possible to classify the general requirements that a caloric material must possess in order to be suitable for refrigeration. A caloric refrigerant should be:

- with high caloric effect and thermal conductivity, low specific heat in the working temperature range, together with a high corrosion resistance to guarantee good energy performances;
- toxic element free and chemically stable from a health and safety point of view;
- easily synthesizable, composed by a restricted number of elements and inexpensive to ensure reproducibility in large-scale applications.

Gschneidner Jr. and V. K. Pecharsky introduced [51] in 2000 relative cooling power, a useful parameter for estimating the cooling capacity of magnetocaloric materials taking into account significative variables like the amplitude of MCE in correspondence of its peak temperature and the wideness of the effect by counting the full width at half maximum (ΔT_{FWHM}). Relative cooling power could be generalized for all caloric materials and expressed with reference to isothermal entropy or adiabatic temperature changes, respectively as:

$$RCP(s) = -\Delta s_{MAX} * \Delta T_{FWHM} \quad (9)$$

$$RCP(T) = -\Delta T_{ad,MAX} * \Delta T_{FWHM} \quad (10)$$

In the present investigation materials belonging to the four main classes of caloric effect materials have been considered. Following they are introduced more detailed.

4.1 Magnetocaloric materials

Four are the magnetocaloric materials tested; they can be considered the most promising material in the temperature range. Gadolinium is for sure the first candidate since it has represented the benchmark [52,53] from the dawn of the researches on magnetic cooling. It is a lanthanide rare-earth material that shows the MCE maximum at 294 K where a second order transition arises. Type $Gd_5(Si_{1-x}Ge_x)_4$ (where $0 < x < 0.5$) alloys are worthy of consideration [54] as well, because of the Giant MCE manifesting in room temperature range. In particular, $Gd_5Si_2Ge_2$ is the best candidate of this family of alloys for its two MCE peaks (at 276 K and 299 K) [55]. $LaFe_{11.384}Mn_{0.356}Si_{1.26}H_{1.52}$ [56] and $LaFe_{11.05}Co_{0.94}Si_{1.10}$ [57] exhibiting peaks at 290 K and 287 K, respectively, are the two materials under test belonging to the rare earth transition metals $La(Fe_xSi_{1-x})_{13}$ [58], an interesting class for materials reproducibility, price and ecotoxicity. Table 2 reassumes the MCE characteristics of them.

MCE Material	T_{peak} [K]	ΔB [T]	ΔT_{ad} [K]	ρ [kg/m^3]	K [W/mK]	RCP(s) [J/kg]	RCP(T) [K^2]	Ref.
Gd	294	1.5	6	7900	10.9	240	187	[52]
$Gd_5Si_2Ge_2$	276	1.5	14	7205	5.8	154	117	[54]
$LaFe_{11.384}Mn_{0.356}Si_{1.26}H_{1.52}$	290	1.5	5	7100	9	115	50	[56]
$LaFe_{11.05}Co_{0.94}Si_{1.10}$	287	1.5	5.5	7290	8.9	83	30	[57]

Table 2. Thermodynamic and caloric features of MCMs under investigation.

4.2 Electrocaloric materials

The number of electrocaloric candidates of the present study is bigger than magnetocaloric one because larger is the number of potential electrocaloric refrigerants. As a matter of fact, the scientific community has made many efforts [59, 60] in developing performing and competitive ECE solid-state materials for room temperature refrigeration. The ECE materials selected and introduced in this paper belong to different

physical categories: single-crystal, ceramics or polymer, in bulk substrates or else thick or thin films. Among them particular importance is assumed by the class of P(VDF-TrFE-CFE)/BSTs polymer nanocomposities [61] because of the large ECE manifested. P(VDF-TrFE-CFE)/BSTs polymer nanocomposities [62] have been selected, for their high ECE, since they are implemented by doping the polymer P(VDF-TrFE-CFE) 62.3/29.9/7.8 mol% with ($Ba_xSr_{1-x}TiO_3$), with the purpose to reduce both dimensions of the ferroelectric domain and the energy bandgap to phase transition. In particular, for the enhanced ECE detected in the room temperature range, under not so elevated electric field variations (75 $V*\mu m^{-1}$) the tested materials belonging to the above class are: P(VDF-TrFE-CFE) 62.3/29.9/7.8- $Ba_{0.67}Sr_{0.33}TiO_3$, P(VDF-TrFE-CFE) 62.3/29.9/7.8-$Ba_{0.71}Sr_{0.29}TiO_3$, P(VDF-TrFE-CFE) 62.3/29.9/7.8-$Ba_{0.74}Sr_{0.26}TiO_3$, P(VDF-TrFE-CFE) 62.3/29.9/7.8-$Ba_{0.77}Sr_{0.23}TiO_3$, that following will be referred more compactly as P(VDF-TrFE-CFE)/BST67, P(VDF-TrFE-CFE)/BST71, P(VDF-TrFE-CFE)/BST74, P(VDF-TrFE-CFE)/BST77.

0.93PMN-0.07PT thin film [63] has been considered because of its giant electrocaloric effect around 300 K. The material grows up by filling the relaxor ceramic $PbMg_{2/3}Nb_{1/3}O_3$ (PMN) with $PbTiO_3$ (PT), to achieve a wide-range of dipolar ordering [64]. Moreover, also the stand-alone bulk sample of $PbTiO_3$ has been employed as caloric refrigerant, for its multicaloric nature [65] (it shows both and simultaneously electrocaloric and elastocaloric effect in the room temperature range). Even if its caloric peaks are quite further (750 K) from room temperature range, $PbTiO_3$ provides promising values of ΔT_{ad} around 300 K at moderate fields. With reference to electrocaloric effect, $PbTiO_3$ has been employed considering ΔE= 100 MVm^{-1}.

Considering the $Pb_{1-3x/2}La_xZr_{0.85}Ti_{0.15}O_3$ (PLZT) class in thick films shape, the single composition PLZT 11/85/15 [66], which shows an ECE peak of ΔT_{ad} = 12 K under ΔE=90MVm^{-1}, has been tested. The "up-graded" and the "down-graded" antiferroelectric compositions have also been employed [67]; they have been obtained, respectively, by increasing or decreasing the La content from 8 to 14 mol%. They show an enormous ECE at room temperature. Moreover, the giant ECE (ΔT_{ad} = 45.3 K at 598 $kVcm^{-1}$) in relaxor ferroelectric $Pb_{0.8}Ba_{0.2}ZrO_3$ (PBZ) [68] thin film has been tested. The latter material has been fabricated on the Pt(111)/TiO_x/SiO_2/Si substrate by a sol-gel method. In this material nano-scaled AntiFerroElectric (AFE) and FerroElectric (FE) phases coexist at room temperature (290 K) rather than at its Curie temperature (408 K). Lastly, a 2 mm-$Pb_{0.97}La_{0.02}(Zr_{0.75}Sn_{0.18}Ti_{0.07})O_3$ (PLZST) AntiFerroElectric (AFE) thick film with a tetragonal structure deposited on $LaNiO_3$/Si (100) substrates [69], has been investigated because of its giant ECE shown in the range from 278 to 298 K. Table 3 lists all the properties and features of the EC materials included in the investigation.

ECE Material	**T_{peak} [K]**	**ΔE [MV/m]**	**ΔT_{ad} [K]**	**ρ [kg/m^3]**	**k [W/mK]**	**RCP(s) [J/kg]**	**RCP(T) [K^2]**	**Ref.**
P(VDF-TrFE-CFE)/BST67	311	75	9.2	2060	10.9	10550	1087	[62]
P(VDF-TrFE-CFE)/BST71	322	75	9.4	2060	5.8	10000	1038	[62]
P(VDF-TrFE-CFE)/BST74	331	75	9.7	2030	9	4065	50	[62]

P(VDF-TrFE-CFE)/BST77	337	75	9.9	2060	8.9	4180	30	[62]
0.93PMN-0.07PT	298	50.9	9	8300	1.4	135	125	[63]
		72.3	13			162	160	
PbTiO3	750	100	35	8000	4	4450	17500	[65]
PLZT11/85/15	111	90	12	7900	1.9	1200	1320	[66]
PLTZ upgraded	/	90	28	7900	1.9	3300	2800	[67]
PLTZ downgraded	/	90	20	7900	1.9	1380	1200	[67]
$Pb_{0.8}Ba_{0.2}ZrO_3$	290	59.8	45	7700	1	480	630	[68]
		40.8	36			288	324	
		21	20			120	140	
$Pb_{0.97}La_{0.02}(Zr_{0.75}Sn_{0.18}Ti_{0.07})O_3$	278	90	54	8300	1	-	-	[69]
		70	43			-	-	
		60	33			-	-	

Table 3. Thermodynamic and caloric features of ECMs under investigation.

4.3 Elastocaloric materials

Most of the materials showing elastocaloric effect are also called shape memory materials, due to the shape-memory effect (they remember the original shape and can return to the pre-deformed shape). Shape-memory materials are cubic intermetallic which show superelastic mechanical properties inherent to the first-order transition (austenitic-martensitic) that they experience: the transition sees the materials passing from high to lower symmetry and temperature as a consequence of the lattice deformations [70]. If the transition comes out by the imposition of uniaxial stress, a prominent elastocaloric effect occurs. In this investigation the choice of the promising elastocaloric refrigerants range has fallen upon three different materials which show giant eCE in room temperature range:

- single crystal of Cu-Zn-Al: particularly $Cu_{68.13}Zn_{15.74}Al_{16.13}$ [71] which, for a stress varying in [0;140] MPa range, exhibits high values of ΔT_{ad} (around 16 K) in the room temperature range of interest.
- Ni-Ti polycrystals due to superelastic behaviour that, if driven by uniaxial stress of $\Delta\sigma$ = 900 MPa, show a maximum ΔT_{ad} of about 25 K at 350 K [72].
- The relaxor multicaloric $PbTiO_3$ [64], already introduced in section 4.2, and here tested under $\Delta\sigma$ = 2 GPa.

Table 4 contains the details about the elastocaloric candidates considered.

eCE Material	**T_{peak} [K]**	**$\Delta\sigma$ [GPa]**	**ΔT_{ad} [K]**	**ρ [kg/m^3]**	**k [W/mK]**	**RCP(s) [J/kg]**	**RCP(T) [K^2]**	**Ref.**
$Cu_{68.13}Zn_{15.74}Al_{16.13}$	234	0.14	16.5	7700	179	-	-	[71]
NiTi	350	0.9	26	6500	10	1800	1250	[72]
$PbTiO_3$	630	2	34	8000	4	5000	6125	[65]

Table 4. Thermodynamic and caloric features of eCMs under investigation.

4.4 Barocaloric materials

In the number of barocaloric candidates for room temperature refrigeration, an interesting comparison has been done. As a matter of fact, the investigation has focused upon two distinct materials:

- the $(NH_4)_2MoO_2F_4$ oxyfluorides [73], direct BCE material, whose T_{peak} is about located around 272 K considered for three different pressure fields applied;
- the hexagonal Ni_2In-type $MnCoGe_{0.99}In_{0.01}$ [74] exhibiting an inverse barocaloric effect due to a pressure-driven orthorhombic-hexagonal magneto-structural transition. The transition for $MnCoGe_{0.99}In_{0.01}$ occurs around 298 K with a ΔT_{ad} of -18.3 K.

Table 5 contains details about the two tested barocaloric materials.

BCE Material	**T_{peak} [K]**	**Δp [GPa]**	**ΔT_{ad} [K]**	**ρ [kg/m^3]**	**k [W/mK]**	**RCP(s) [J/kg]**	**RCP(T) [K^2]**	**Ref.**
$(NH_4)_2MoO_2F_4$	272	0.9	18	2200	1	792	873	[73]
	272	0.7	15			548	562	
	272	0.5	12			410	420	
$MnCoGe_{0.99}In_{0.01}$	298	0.3	-18.3	7900	65	840	225	[74]

Table 5. Thermodynamic and caloric features of BCMs under investigation.

4.5 Building Q-functions for caloric effect in the model

The experimental data proper of the caloric materials presented in sections 4.1-4.4 have been manipulated (as described in section 3.2) to the purpose of building mathematical Q-functions to be employed in the ACR 2-D model. For all the caloric effects, the hysteresis phenomenon has been taken in consideration by means of the following considerations:

I) for the materials for which two different ΔT_{ad}(field,T) curves (i.e. for field increasing and decreasing cycles) were available in scientific literature, two separate Q-functions have been built;

II) where two separate ΔT_{ad}(field,T) for field increasing/decreasing were not reachable, the first Q-function has been built basing on the available ΔT_{ad}(field,T) and the second Q-function has been constructed, shifting the first one along x-axis, according to an aprioristic estimation of the hysteresis phenomenon.

Furthermore, with reference to MCE materials two separate Q-functions have been built for magnetization and demagnetization combining, next to the effect of the hysteresis existing in the first-order transition materials considered, also the variability of heat capacity C(B,T). The latter, for all the other caloric effect materials, has been considered constant [44].

As an example, in the figures 4-7 are shown some significative Q-functions for the four caloric effect materials.

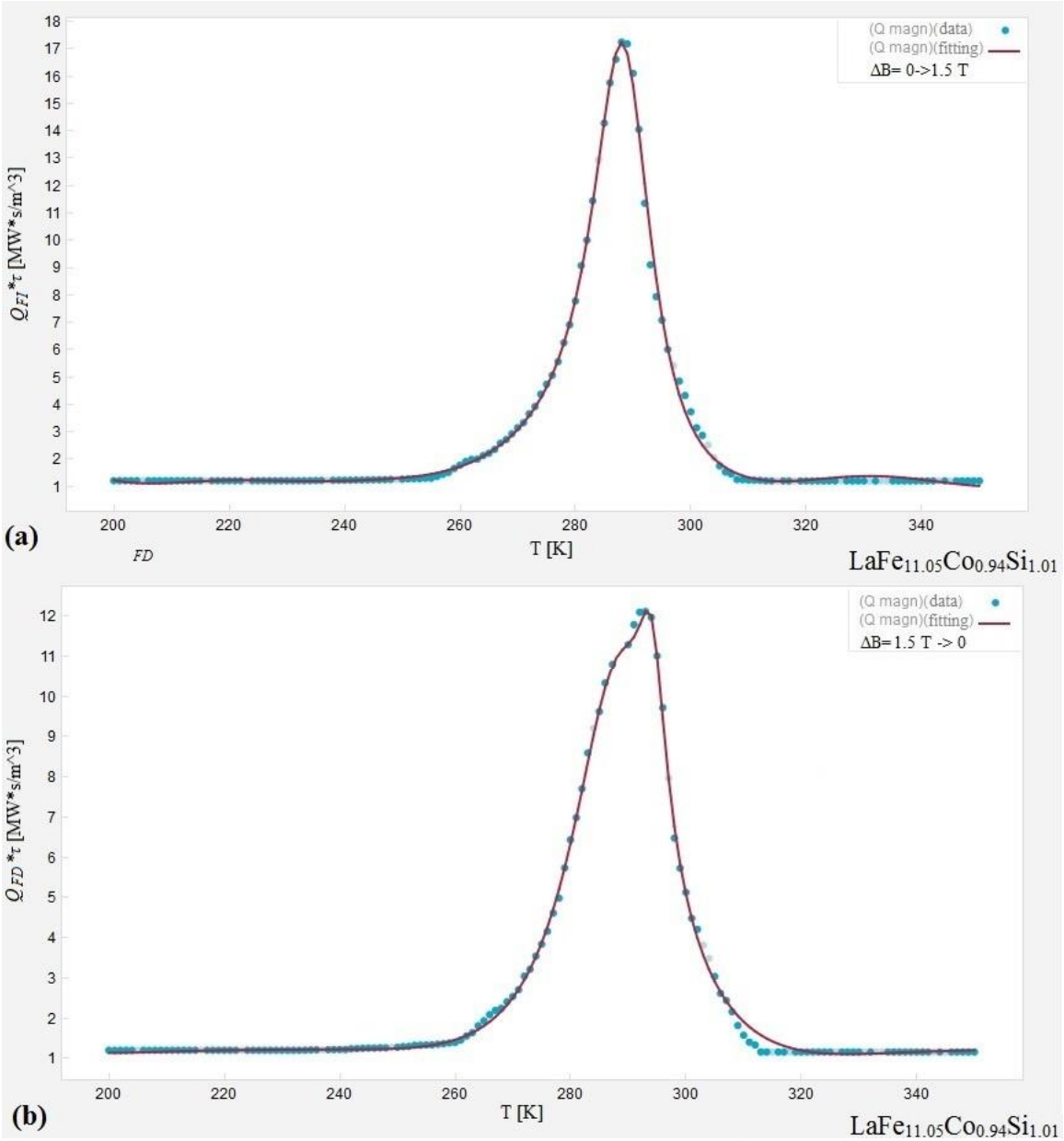

Figure 4. Q-functions built for the magnetocaloric material $LaFe_{11.05}Co_{0.94}Si_{1.10}$ for (a) magnetization and (b) demagnetization processes in the range 0÷1.5 T.

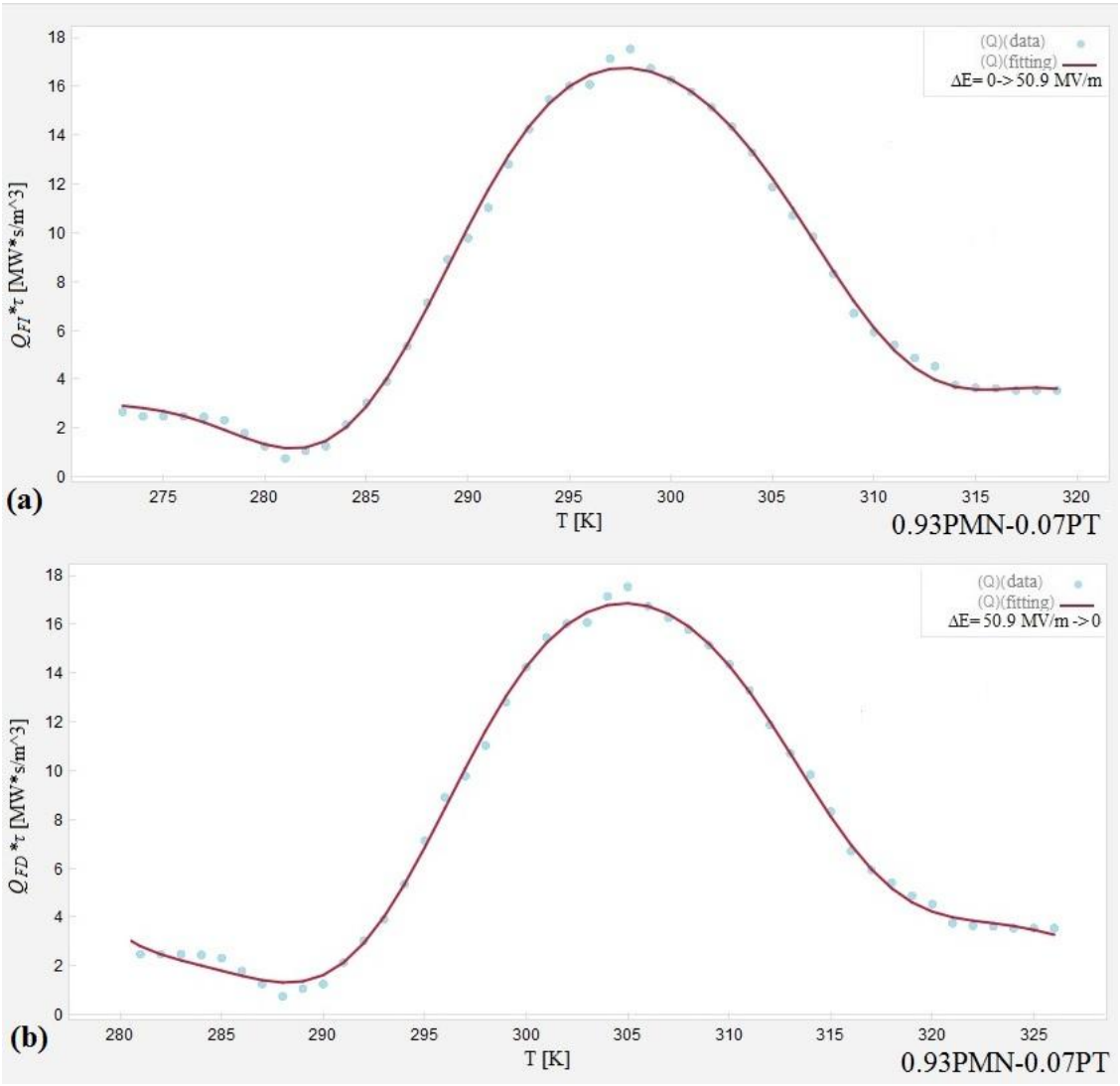

Figure 5. Q-functions built for the electrocaloric 0.93PMN-0.07PT for: (a) polarization; (b) depolarization processes under a field changing in 0÷50.9 MV/m.

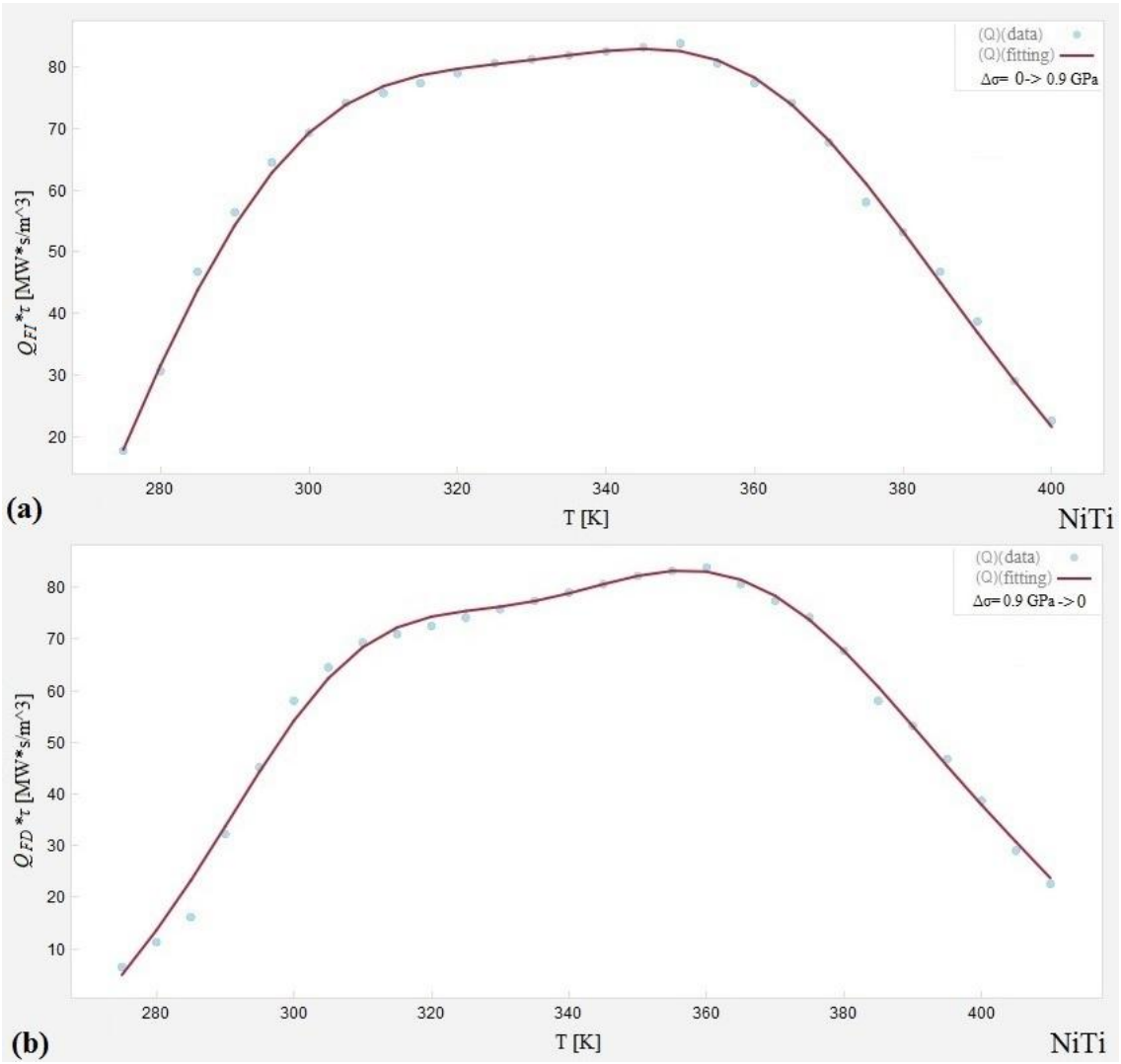

Figure 6. Q-functions built for the elastocaloric material NiTi for (a) loading and (b) unloading processes in the range 0÷0.9 GPa.

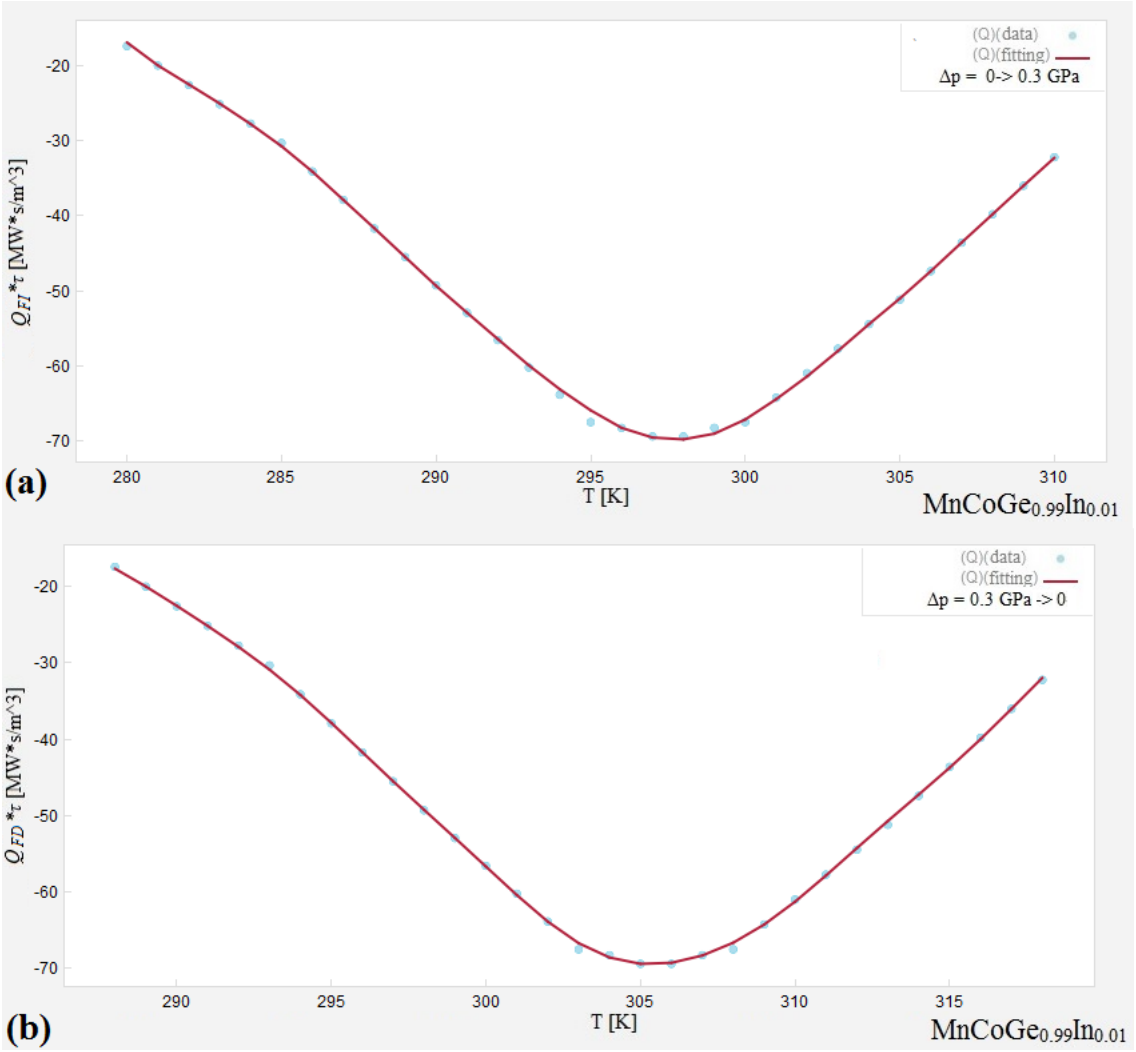

Figure 7. Q-functions built for the inverse barocaloric $MnCoGe_{0.99}In_{0.01}$ for field: (a) increasing; (b) decreasing in the range 0÷0.3 GPa.

In Table 6 are reported the Q_{FI} *τ functions, related to the field increasing process, obtained starting from the experimental data.

Material	Mathematical expression
MCE materials	
Gd ΔB=1.5 T	$Q_{FI} * \tau = 10^6 \left\{0.4261 + 2.222\cos(2.145 + 0.03856\,T) + \frac{2.848}{\cos[5.711 - 0.3543\cos(-0.1063\,T) - 0.4261\cos(-0.06519\,T)] + \cos(-0.06519\,T)}\right\}$
$Gd_5(Si_2Ge_2)$ ΔB=1.5 T	$Q_{FI} * \tau = 10^6 * [0.877 + \frac{142 - 0.439T_s}{5.15 - 4.82 * \sin(37.9T_s)}]$
$LaFe_{11.384}Mn_{0.356}Si_{1.26}H_{1.52}$ ΔB=1.5 T	$Q_{FI} * \tau = 10^6 * [9.85 + 0.0376T\cos(-31.2T) + \cos(5.52T)\cos(-31.2T) + \cos(5.52T) - 3.35 * \sin(-0.349T)]$
$LaFe_{11.05}Co_{0.94}Si_{1.01}$ ΔB=1.5 T	$Q_{FI} * \tau = 10^6 * [\frac{2.04 + 0.516\sin(-6.17T)}{1.14 + \cos(0.28\sin(-12.7T) - 0.0549T)}]$
ECE materials	

0.93PMN-0.07PT ΔE=50.9MV/m	$Q_{FI} * \tau = 10^6 * (7.88 - 2.29cos(44.2T) - 7.3\cos(0.137T))$
0.93PMN-0.07PT ΔE=72.3MV/m	$Q_{FI} * \tau = 10^6 * (216 + 5.73\cos(-0.232T) - 0.917T - 81.5\cos(0.0302T))$
P(VDF-TrFE-CFE)/BST67 ΔE=75.0 MV/m	$Q_{FI} * \tau = 10^6 * (3.32 * T + 0.0321 * T * \cos(6420 * T) - 479 - 0.0055 * T^2 - 1.23 * \cos(6420 * T) - 7.81 * \cos(6420 * T))$
P(VDF-TrFE-CFE)/BST71 ΔE=75.0 MV/m	$Q_{FI} * \tau = 10^6 * \left(2.85 * T + \frac{5000 * \cos(0.0871 * T)}{T} - 423 - 0.00455 * T^2 - 17.3 * \cos(0.0871 * T)\right)$
P(VDF-TrFE-CFE)/BST74 ΔE=75.0 MV/m	$Q_{FI} * \tau = 10^6 * (3.35 * \mathrm{T} + 0.885 * \sin(0.118 * \mathrm{T}) + 0.397 * \sin(0.118 * \mathrm{T}) * \sin(0.117 * \mathrm{T}) - 518 - 0.00519 * \mathrm{T}^2)$
P(VDF-TrFE-CFE)/BST77 ΔE=75.0 MV/m	$Q_{FI} * \tau = 10^6 * (3.89 * T - 612 - 0.00594 * T^2 - 1.21 * cos(0.101 * T))$
PLZT11/85/15 ΔE=90.0 MV/m	$Q_{Q_{FI}} * \tau = 10^6 * (18.63 + 4.12 * \cos(3.69 + 0.05 * T) - 4.46 * \cos(3.69 + 0.05 * T) * \cos(3.69 + 0.05 * T))$
PLZT upgraded ΔE=90.0 MV/m	$Q_{FI} * \tau = 10^6 * (370.5 + 1.3 * \cos(0.356 * T) + 0.219 * \cos(376.4 * T) - 1.03 * T - 8.11 * \cos 0.137 * T)$
PLZT downgraded ΔE=90.0 MV/m	$Q_{FI} * \tau = 10^6 * (53 + 15.73 * \sin(-0.063 * T))$
$PbTiO_3$ ΔE=100.0 MV/m	$Q_{FI} * \tau = 10^6 * [4.83 + 0.000118 * T^2]$
$Pb_{0.8}Ba_{0.2}ZrO_3$ ΔE=21.0 MV/m	$Q_{FI} * \tau = 10^6 * [23.44 - \cos(\mathrm{T}) - 6 * \cos(0.5094 * \mathrm{T}) - 16.17 * \sin(-6.527 * \mathrm{T})]$
$Pb_{0.8}Ba_{0.2}ZrO_3$ ΔE = 40.8 MV/m	$Q_{FI} * \tau = 10^6 * [700.6 + 1.773 * T * \sin(5.775 + 0.3637 * T) + 7.199 * \sin(0.3637 * T) * \sin(5.775 + 0.3637 * T) - 2.24 * T - 542.1 * \sin(5.773 + 0.3637 * T)]$
$Pb_{0.8}Ba_{0.2}ZrO_3$ ΔE = 59.8 MV/m	$Q_{FI} * \tau = 10^6 * [682.9 + 2.362 * \mathrm{T} * \sin(3.58 + 0.372 * \mathrm{T}) - 2.141 * \mathrm{T} - 719.1 * \sin(3.572 + 0.372 * \mathrm{T})]$
$Pb_{0.97}La_{0.02}(Zr_{0.75}Sn_{0.18}Ti_{07})O_3$ ΔE=90.0 MV/m	$Q_{FI} * \tau = 10^6 * [0.2746 * \mathrm{T} + (\frac{2.187 * 10^5}{T - 720.1})]$
$Pb_{0.97}La_{0.02}(Zr_{0.75}Sn_{0.18}Ti_{07})O_3$ ΔE=70.0 MV/m	$Q_{FI} * \tau = 10^6 * [616.7 - 1.825 * \mathrm{T} - 3.64 * \cos(0.15 * \mathrm{T})]$
$Pb_{0.97}La_{0.02}(Zr_{0.75}Sn_{0.18}Ti_{07})O_3$ ΔE=60.0 MV/m	$Q_{FI} * \tau = 10^6 * [0.8306 * \mathrm{T} + (\frac{2.017 * 10^5}{T - 869.5})]$
<u>eCE materials</u>	
NiTi Δσ=0.9 GPa	$Q_{FI} * \tau = 10^6 * [3662 - \frac{59560}{T} - 5.37 * \mathrm{T} - 3.948 * \cos(134.6 * T)]$
$Cu_{68.13}Zn_{15.74}Al_{16.13}$ Δσ=0.14 GPa	$Q_{FI} * \tau = 10^6 * [849 + 34.7 * \sin(0.000147 * T^2) + \sin(0.438 * T) - 2.73 * T]$
$PbTiO_3$ Δσ=2 GPa	$Q_{FI} * \tau = 10^6 * [7.58 + 0.000139\, T^2]$
<u>BCE materials</u>	
$NH_4)_2MoO_2F_4$ Δp = 0.5 GPa	$Q_{FI} * \tau = 10^6 * [133.4 + 10.7 * \cos(351.5 * \mathrm{T}) - 0.3822 * \mathrm{T} - 0.03769 * \mathrm{T} * \cos(351.5 * \mathrm{T})]$

$(NH_4)_2MoO_2F_4$ $\Delta p = 0.7$ GPa	$Q_{FI} * \tau = 10^6 * [[1.088 + 0.2777 * \cos(0.3995 * T) - 85.38 - 0.002365 * T^2]$
$(NH_4)_2MoO_2F_4$ $\Delta p = 0.9$ GPa	$Q_{FI} * \tau = 10^6 * [96.92 + 0.4259 * \sin(0.2341 * T) - 0.2063 * T]$
$MnCoGe_{0.99}In_{0.01}$ $\Delta p = 0.3$ GPa	$Q_{FI} * \tau = 10^6 * [-31.83 - 34.34 * \cos(0.0002128 * T^2)]$

Table 6. Mathematical expressions for the $Q_{FI} * \tau$ functions, related to the field increasing process.

5. Investigation and results

The investigation has been performed simulating several ACR cycles for the above described caloric materials. The ranges where external applied fields vary are related to the particular caloric material under test and they are explicated in Tables 2-5. Fixed are: the active caloric cycle frequency (1.25 Hz), cold and hot heat exchanger temperature (T_C=292 K, T_H=300 K) while mass flux was varied in the range 150 ÷ 250 kg $s^{-1}m^{-2}$. Such operating conditions are the same for all the class of caloric materials in order to build a general map of performance for caloric cooling. Therefore, the purpose of the investigation introduced is to compare the energy performances of the ACR regenerator while it employs one by one the caloric refrigerants. The energy parameters evaluated are the followings:

$$\Delta T_{span} = T_H - \frac{1}{\tau}\int_{3\tau+n\theta}^{4\tau+n\theta} T_f(0,y,t)\,dt \tag{11}$$

ΔT_{span} quantifies the temperature span across the active caloric regenerator at the end of a steady-state hot-to-cold flow step.

Cooling power measures the power at which the cooling system removes heat:

$$\dot{Q}_{ref} = \frac{1}{\theta}\int_{3\tau+n\theta}^{4\tau+n\theta} \dot{m}_f C_f\left(T_C - T_f(0,y,t)\right) dt \tag{12}$$

Coefficient of performances is evaluated as:

$$COP = \frac{\dot{Q}_{ref}}{\dot{Q}_{rej} - \dot{Q}_{ref} + \dot{W}_p} \tag{13}$$

where $\dot{Q}_{rej}$ and $\dot{W}_p$ are estimated as:

$$\dot{Q}_{rej} = \frac{1}{\theta}\int_{\tau+n\theta}^{2\tau+n\theta} \dot{m}_f C_f\left(T_f(L,y,t) - T_H\right) dt \tag{14}$$

$$\dot{W}_p = \frac{\dot{m}(\Delta p_{CF} + \Delta p_{HF})}{\eta_p \rho_f} \tag{15}$$

The energy performances of the modelled ACR regenerator are presented in this section. Figure 8 contains the ΔT_{span} vs G_f graph for a) magnetocaloric, b) electrocaloric, part I, c) electrocaloric, part II, d) elastocaloric and e) barocaloric materials, estimated under the above-mentioned operative conditions. The first tendency emerged from the investigation is the inverse proportionality between fluid velocity and ΔT_{span}:

corresponding to small fluid flow rate, the fluid is regenerated to reach lower cold side temperatures. From the plotted data, one can notice that for most of the caloric materials tested ΔT_{span} follow within the range 10 ÷ 17 K. Among magnetocaloric materials, gadolinium offers the highest temperature spans with a middle value of 10.2 K; such data were predictable since it works in a temperature range centred to its Curie point (294 K). All the other MCE candidates underperform Gd with a negative primacy of $Gd_5Si_2Ge_2$ whose ΔT_{span} is on average 15% lower than the former. Indeed, this material works in a temperature range out of its Curie temperature (276K). Temperature spans of MCMs remain very low if they are compared to the other caloric classes and this is also due to limited magnetic field obtainable by permanent magnets. In the group of mechanocaloric materials the trends are slightly better since the lowest ΔT_{span} (10.9 K for G_f=250 kg m^{-2} s^{-1}), registered for $PbTiO_3$, is however greater than Gd ones. Peaks are exhibited by the eCE Ni-Ti polycrystals driven by uniaxial stress of $\Delta\sigma$ = 900 MPa, with a middle value of 15.5 K and by the inverse BCE materials $MnCoGe_{0.99}In_{0.01}$ (Δp=0.3 GPa) with a peak of 15.3K for G_f = 150 kg m^{-2} s^{-1}. From figure 8(b), one can observe that temperature spans proper of most of ECE materials are lower than those of mechanocaloric materials, but higher than those of gadolinium (and therefore of MCM group): ΔT_{span} of $Pb_{0.8}Ba_{0.2}ZrO_3$ driven by ΔE=21.0 MV m^{-1} are, on average, 16% higher than Gd ones. Positive exceptions are represented by $Pb_{0.8}Ba_{0.2}ZrO_3$ driven by greater electric fields and by ECE materials plotted in figure 4c; for them the ΔT_{span} fall within the range 18-45 K. In particular, $Pb_{0.97}La_{0.02}(Zr_{0.75}Sn_{0.18}Ti_{0.07})O_3$ show giant values of ΔT_{span} (greater than 40K) under so not elevated changes of electric fields applied; as an example on equal ΔE = 90 MV m^{-1}, $Pb_{0.97}La_{0.02}(Zr_{0.75}Sn_{0.18}Ti_{0.07})O_3$ produces a temperature span about 1.8 times greater that PLZT upgraded.

As an example, in the figures 9-10 one can appreciate the temperature profiles built at the end of an ACR cycle operating in steady-state condition, when then the regenerator works with Gadolinium (figures 9) and with PLZT in downgraded composition (figures 10). The plots are referred to the regenerator operating with a mass flux of 198 kg m^{-2} s^{-1}. Particularly, for both the materials the following plots have been built: (a) 2D plot of the whole caloric regenerator; (b) 1D plot vs x-axis for some slices of the regenerator taken on y-axis. From the plots one can visually appreciate the temperature span measured among the two extremities of the regenerator (the cold and the hot one) that is about 10.1 K for gadolinium (figures 9 (a) and (b)) and 20.1 for the electrocaloric PLZT in downgraded composition (figures (a) and (b)).

Figure 11 exhibits Q_{ref} vs G_f trends for a) magnetocaloric, b) electrocaloric, part I, c) electrocaloric, part II, d) elastocaloric and e) barocaloric materials. For each material investigated, cooling power grows with fluid velocity and therefore with mass flux [75].

As already noticed in ΔT_{span} plots, to the magnetocaloric materials are associated the smallest cooling powers. Gadolinium still has the MCM best cooling powers with values in the range 80 - 125 W. The bad primate goes to $Gd_5Si_2Ge_2$ whose $\dot{Q}_{ref}$ do not exceed 30 W the reason has to be found in the temperature working range that is quite far from $Gd_5Si_2Ge_2$ Curie point (276K). The tendencies for mechanocaloric materials see cooling powers going from a minimum of 108 W (evaluated for $PbTiO_3$ driven by uniaxial stress of $\Delta\sigma$ = 2 GPa) to the best results of: i) 450W provided by the eCE NiTi (for $\Delta\sigma$=0.9 GPa and G_f= 250

kg $s^{-1}m^{-2}$); ii) the BCM $(NH_4)_2MoO_2F_4$ which touches a maximum $\dot{Q}_{ref}$ of 400 W (under Δp= 0.9 GPa and G_f = 250), almost 4 times higher than Gd, the best MCE candidate. Also the single crystal $Cu_{68.13}Zn_{15.74}Al_{16.13}$ confers satisfying cooling powers going from 240 W to 420 W. Electrocaloric materials exhibit the same tendency registered for ΔT_{span} evaluation: almost all the materials of figure 9b provide cooling powers comparable to BCM and MCM ones. Moreover, cooling powers of $Pb_{0.8}Ba_{0.2}ZrO_3$ driven by ΔE of 40.8 and 59.8 MV m^{-1} are comparable to NiTi ones. On the other side, electrocaloric materials belonging to group II (figure 11c) deeply overperform all the other caloric candidates with cooling powers between 410 W and 1800 W. The highest $\dot{Q}_{ref}$ peak is associated to $Pb_{0.97}La_{0.02}(Zr_{0.75}Sn_{0.18}Ti_{0.07})O_3$ under ΔE=90 MV m^{-1}.

Coefficients of performances, shown in figure 12 as a function of fluid mass flux for a) magnetocaloric, b) electrocaloric, part I, c) electrocaloric, part II, d) elastocaloric and e) barocaloric materials, do not confirm at all the above described trends. By the results carried out from our investigation, the coefficients of performance associated to the best materials for each caloric category are quite comparable: $Pb_{0.97}La_{0.02}(Zr_{0.75}Sn_{0.18}Ti_{0.07})O_3$ under ΔE=90 MV m^{-1} provides still the highest COP with a maximum of 15 in correspondence of G_f = 250 kg $s^{-1}m^{-2}$ but satisfying are also COPs proper of the elastocaloric Ni-Ti crystal with a value of 11 under an uniaxially driven field change of $\Delta\sigma$ = 0.9 GPa, whereas the best performances among barocaloric candidates are given by $(NH_4)_2MoO_2F_4$ under Δp = 0.9 GPa (COP=10.3 at G_f= 250 kg $s^{-1}m^{-2}$). On the other side, with reference to the MCE materials, although the energetic expenses due to magnetic work are quite narrowed, the smaller cooling powers detected lead to reduced COPs (the highest one is detected with gadolinium, but it does not exceed 9). It is important to underline that the different expense of the work associated with the variation of the driven field has a certain weight. Likewise, also the hysteresis detected in first order transition materials give a certain influence. As already reported in section 4.5, the way we adopted in Q-function building has ensured the account of hysteresis in the evaluation of the energy performances carried out by our investigation. To provide a brief focus of such influence we report, as an example, in figure 13 the energy performances of $Cu_{68.13}Zn_{15.74}Al_{16.13}$ evaluated with and without accounting the hysteresis under an uniaxially driven field changes of $\Delta\sigma$ = 0.14 GPa. From figure 13 (a) one can notice that temperature span does not undergo a strong variation with a maximum reduction of 1 K; on the other side the influence of the hysteresis become more remarkable in cooling powers (figure 13 b) and coefficient of performances (figure 13 c), resulting in an average percentage decrease of -13% for $\dot{Q}_{ref}$ and -18% for COPs.

Indeed, $\dot{Q}_{ref}$ and COPs of many first order transition materials are lower than they would be without considering hysteresis, as noticed also by Zhao et al. [66,67] and Brey et al. [76]. They detected and demonstrated that, among the energy performances, COP is the most sensitive parameter to the presence of significant hysteresis in first order caloric materials.

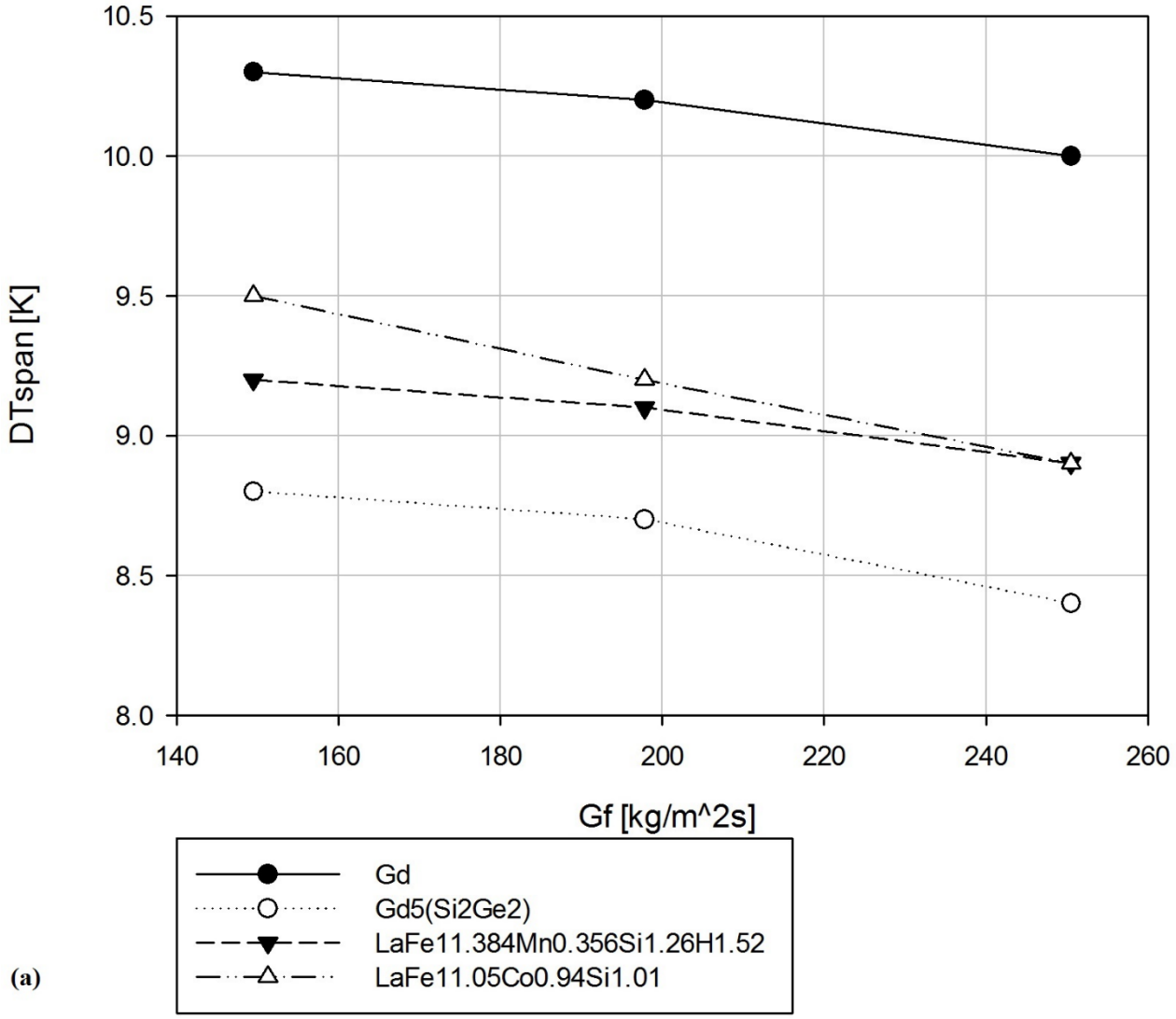
10.5
10.0
9.5
9.0
8.5
8.0
DTspan [K]
140
160
180
200
220
240
260
Gf [kg/m^2s]
Gd
Gd5(Si2Ge2)
LaFe11.384Mn0.356Si1.26H1.52
LaFe11.05Co0.94Si1.01

(a)

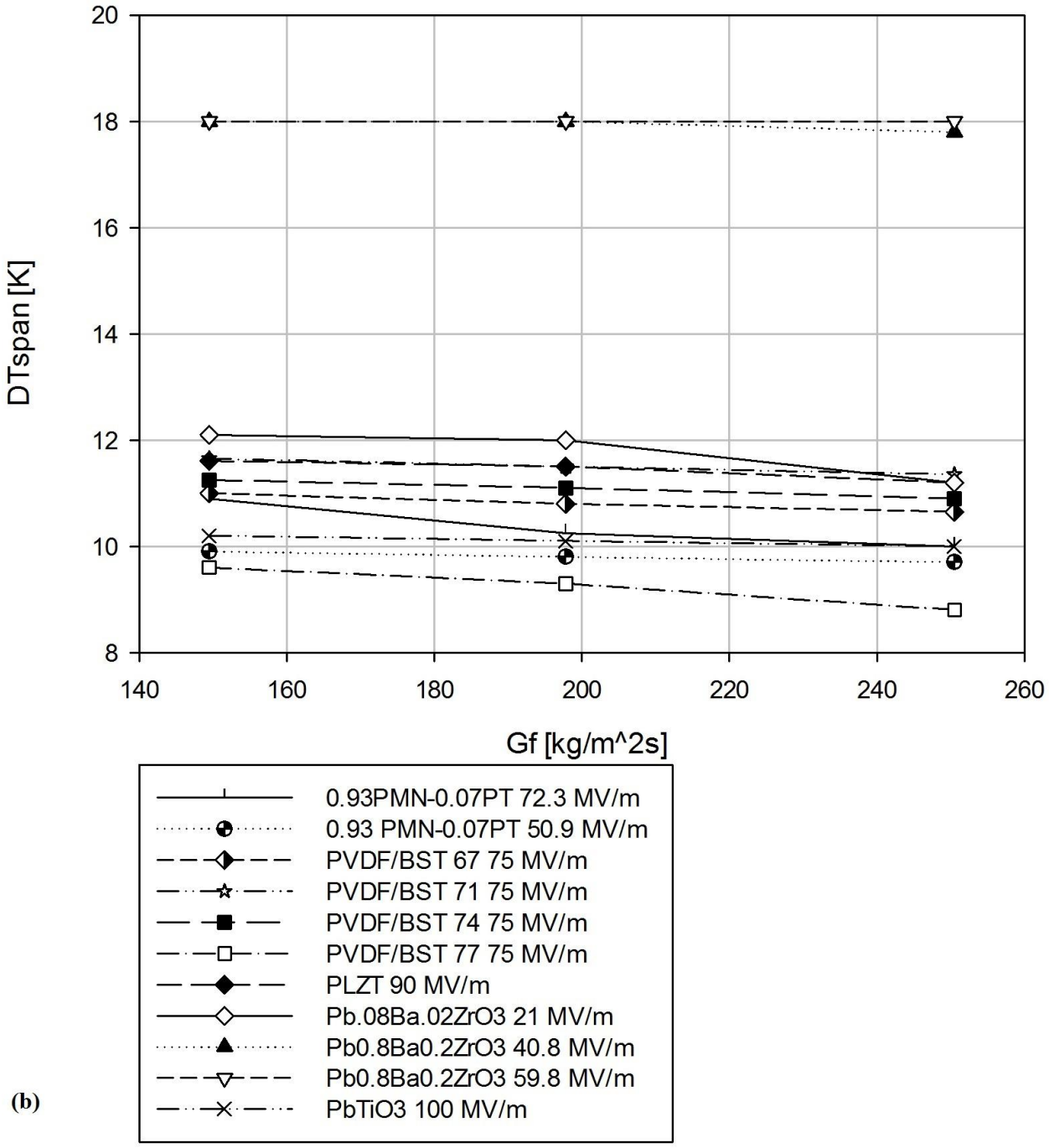
DTspan [K]
Gf [kg/m^2s]
20
18
16
14
12
10
8
140
160
180
200
220
240
260
0.93PMN-0.07PT 72.3 MV/m
0.93 PMN-0.07PT 50.9 MV/m
PVDF/BST 67 75 MV/m
PVDF/BST 71 75 MV/m
PVDF/BST 74 75 MV/m
PVDF/BST 77 75 MV/m
PLZT 90 MV/m
Pb.08Ba.02ZrO3 21 MV/m
Pb0.8Ba0.2ZrO3 40.8 MV/m
Pb0.8Ba0.2ZrO3 59.8 MV/m
PbTiO3 100 MV/m

(b)

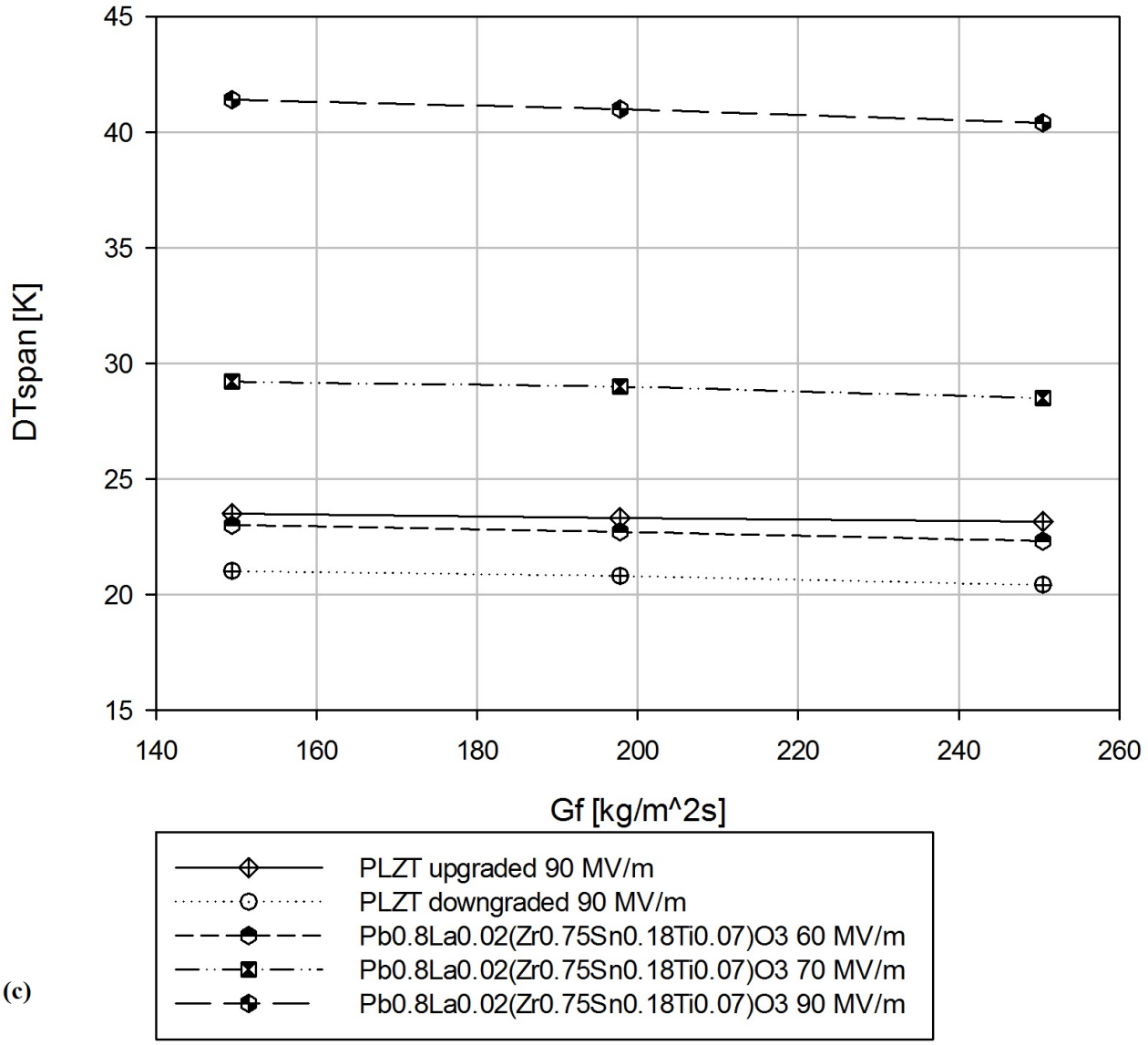
45
40
35
30
25
20
15
DTspan [K]
140
160
180
200
220
240
260
Gf [kg/m^2s]
PLZT upgraded 90 MV/m
PLZT downgraded 90 MV/m
Pb0.8La0.02(Zr0.75Sn0.18Ti0.07)O3 60 MV/m
Pb0.8La0.02(Zr0.75Sn0.18Ti0.07)O3 70 MV/m
Pb0.8La0.02(Zr0.75Sn0.18Ti0.07)O3 90 MV/m

(c)

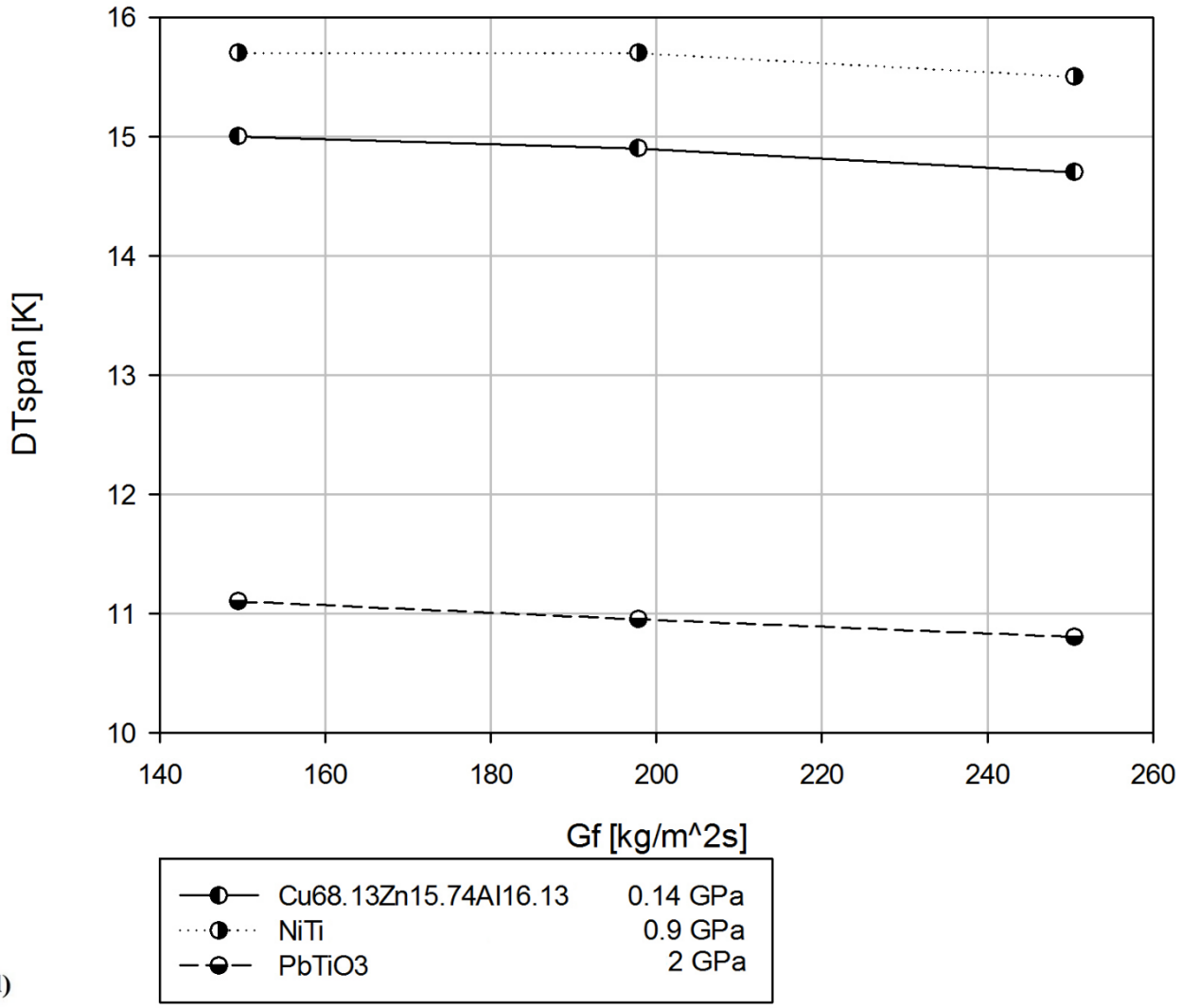
16
15
14
13
12
11
10
DTspan [K]
140
160
180
200
220
240
260
Gf [kg/m^2s]
Cu68.13Zn15.74Al16.13 0.14 GPa
NiTi 0.9 GPa
PbTiO3 2 GPa

(d)

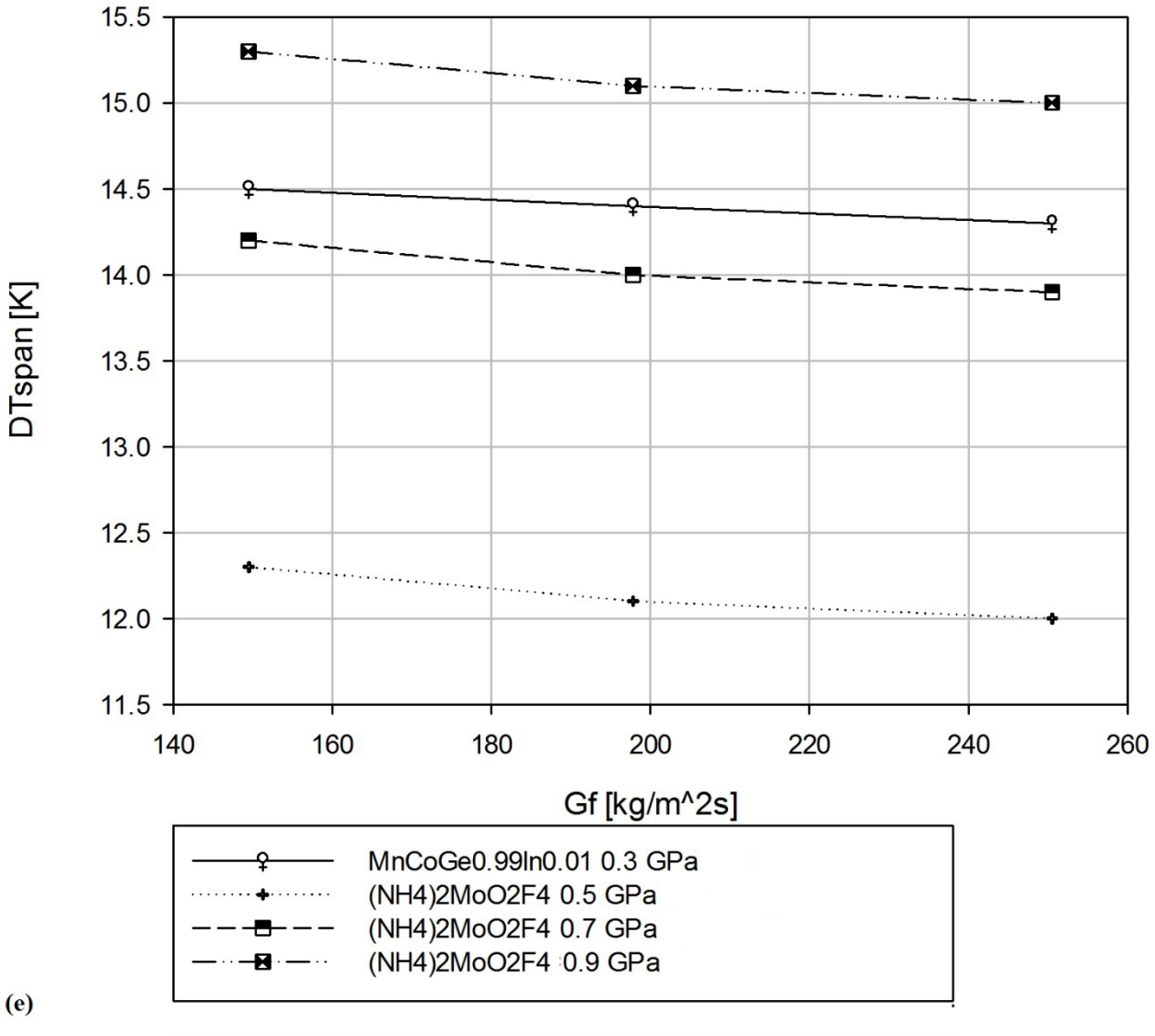

(e)

Figure 8. ΔT_{span} vs mass flux for: (a) magnetocaloric materials under a magnetic field variation ΔB in [0; 1.5] T; (b) the first and (c) the second group of electrocaloric materials; (d) elastocaloric materials; (e) barocaloric materials.

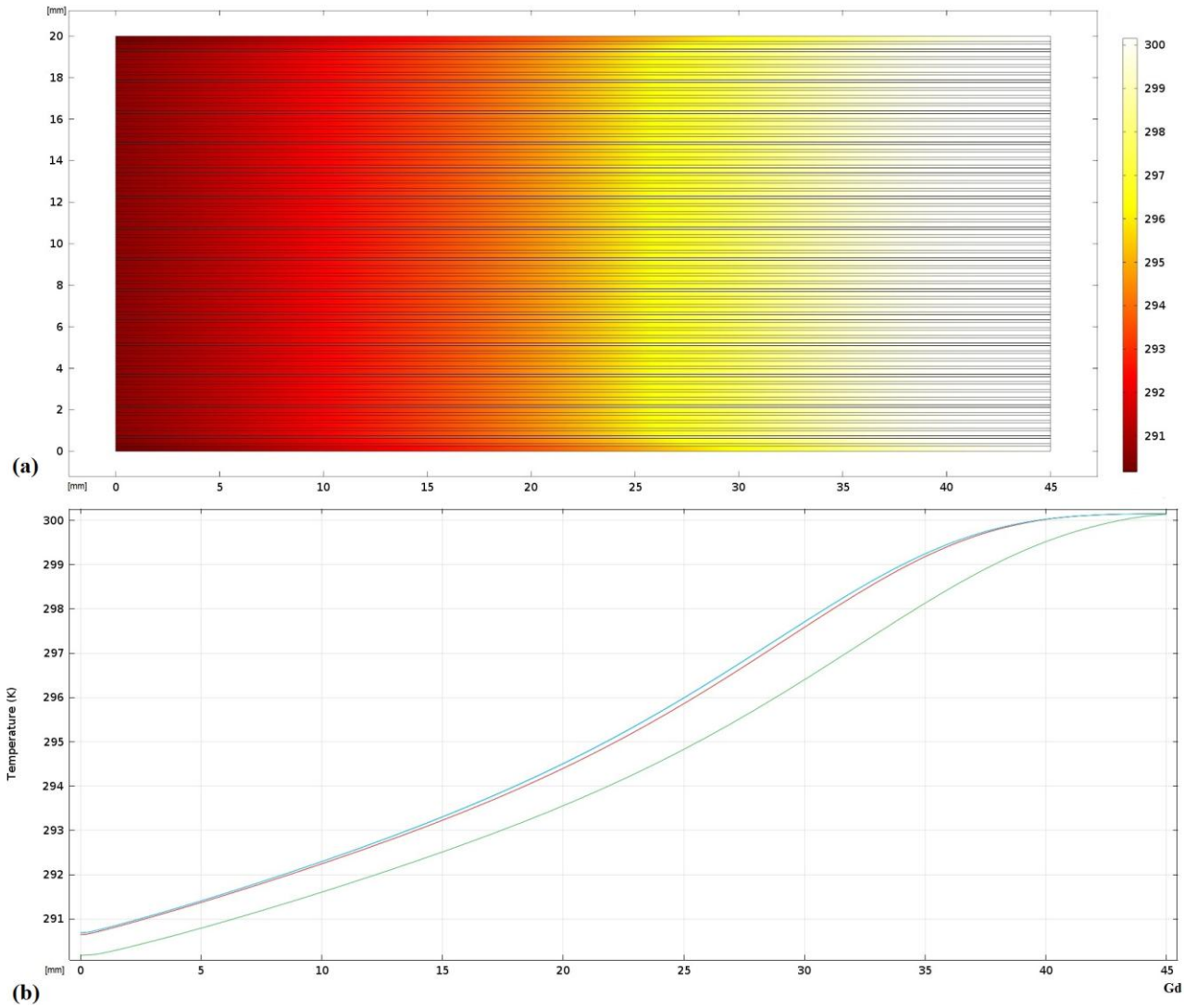

Figure 9. Temperature profiles of the ACR regenerator working with Gd under G_f= 198 kg/m^{2}s: (a) 2D plot of the whole regenerator; (b) 1D plot vs x axis plot vs x-axis for some slices of the regenerator taken on y-axis.

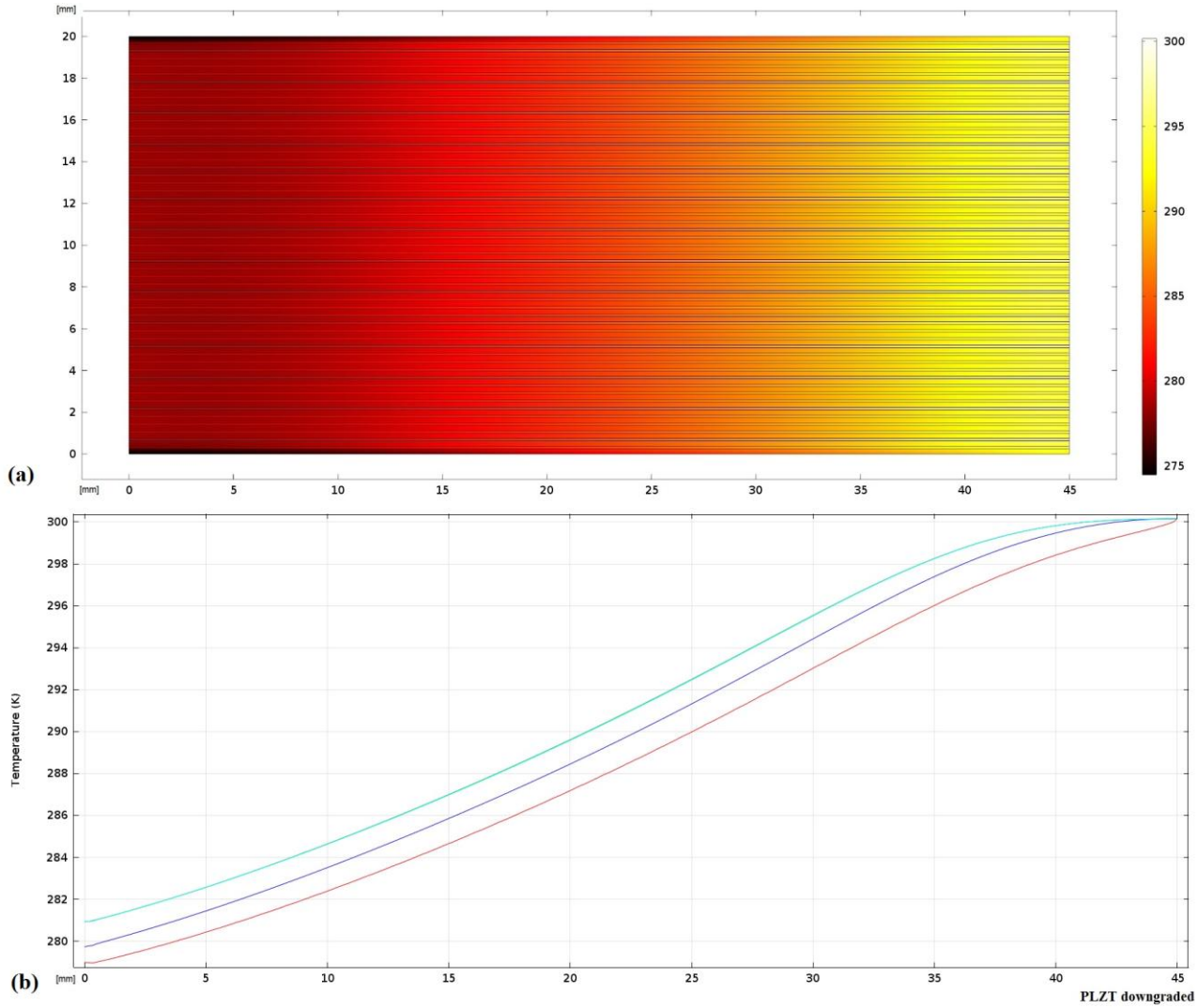

Figure 10. Temperature profiles of the ACR regenerator working with PLZT downgraded under G_f = 198 kg/m^{2}s: (a) 2D plot of the whole regenerator; (b) 1D plot vs x axis plot vs x-axis for some slices of the regenerator taken on y-axis.

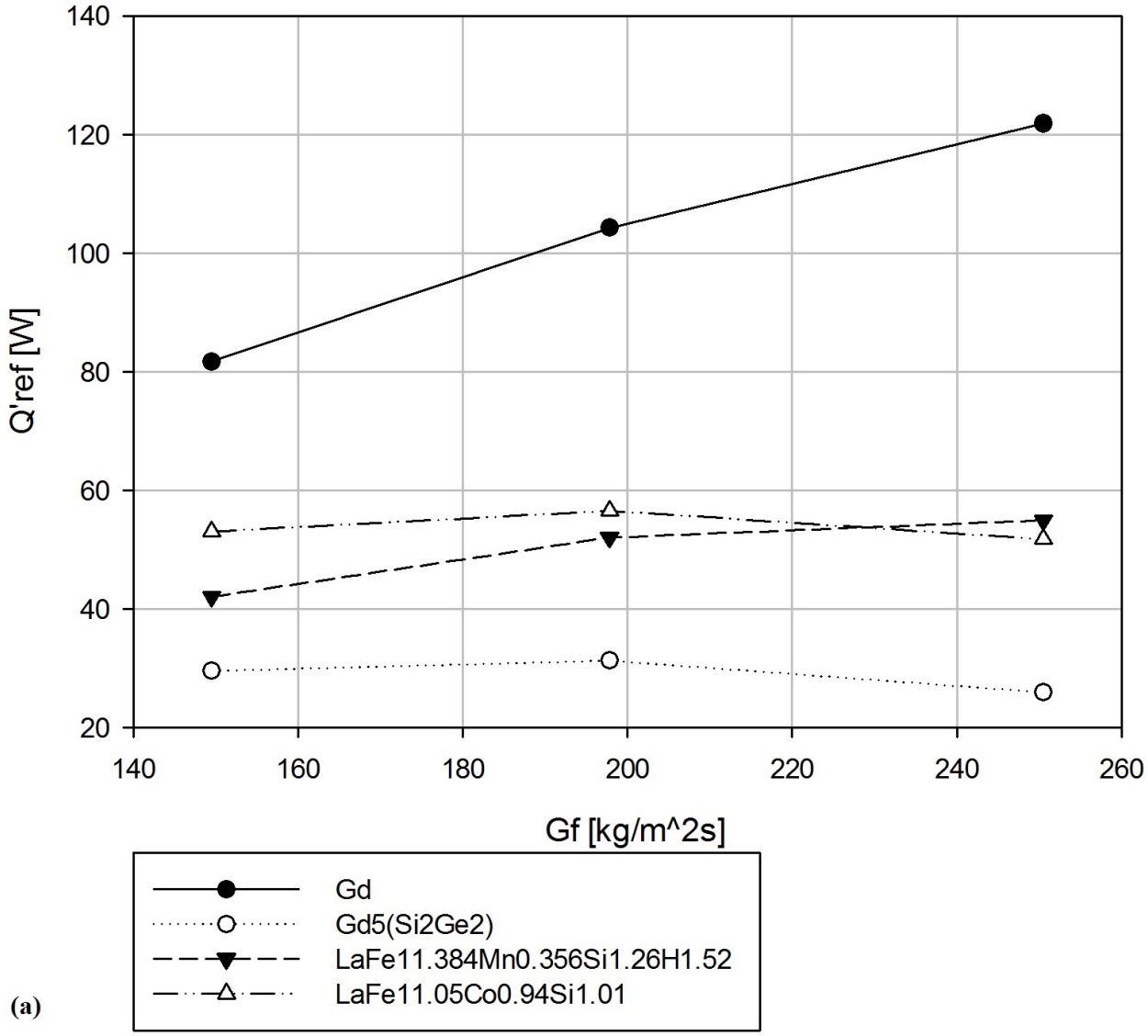
140
120
100
80
60
40
20
Q'ref [W]
140
160
180
200
220
240
260
Gf [kg/m^2s]
Gd
Gd5(Si2Ge2)
LaFe11.384Mn0.356Si1.26H1.52
LaFe11.05Co0.94Si1.01

(a)

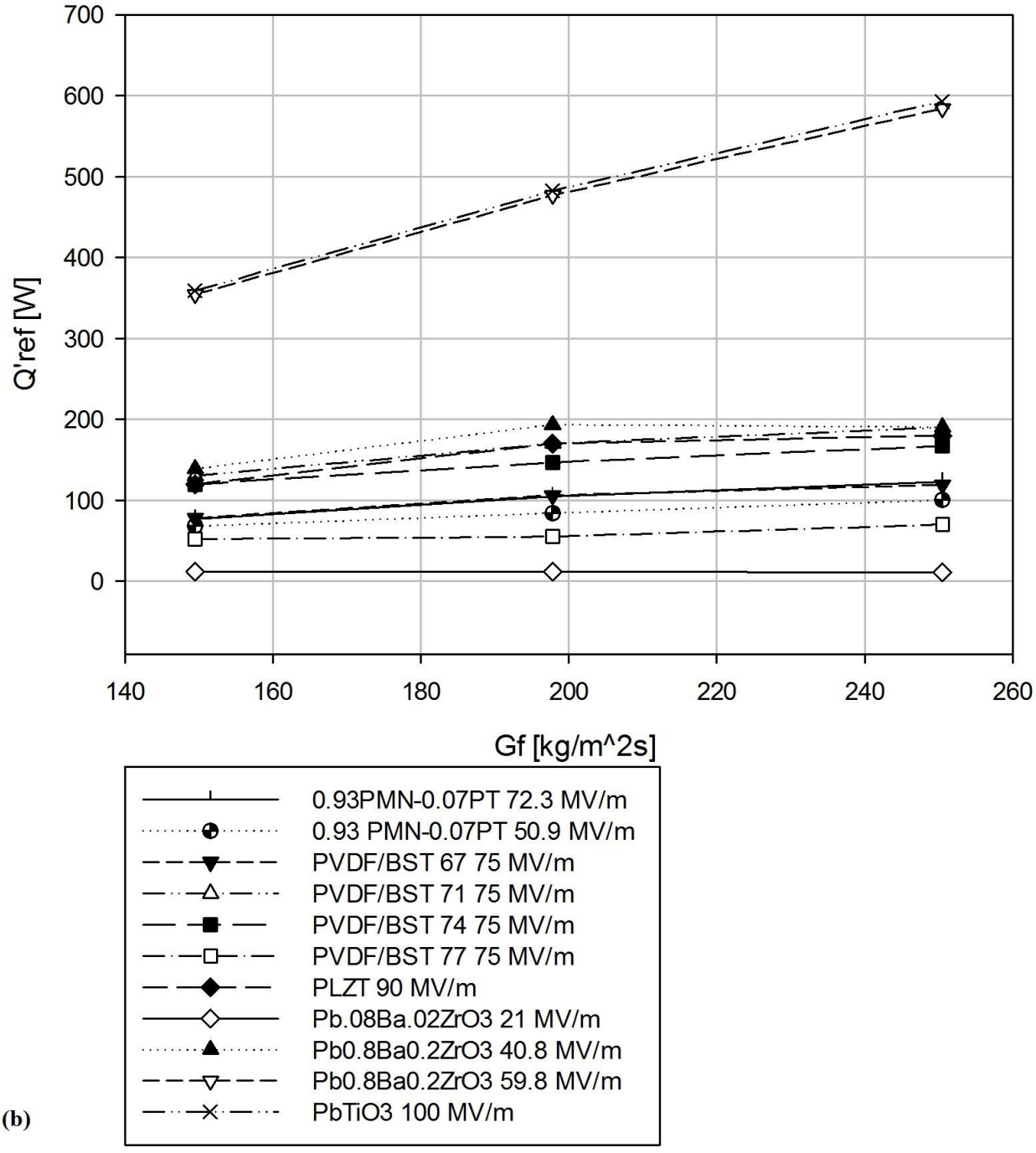
700
600
500
400
300
200
100
0
Q'ref [W]
140
160
180
200
220
240
260
Gf [kg/m^2s]
0.93PMN-0.07PT 72.3 MV/m
0.93 PMN-0.07PT 50.9 MV/m
PVDF/BST 67 75 MV/m
PVDF/BST 71 75 MV/m
PVDF/BST 74 75 MV/m
PVDF/BST 77 75 MV/m
PLZT 90 MV/m
Pb.08Ba.02ZrO3 21 MV/m
Pb0.8Ba0.2ZrO3 40.8 MV/m
Pb0.8Ba0.2ZrO3 59.8 MV/m
PbTiO3 100 MV/m

(b)

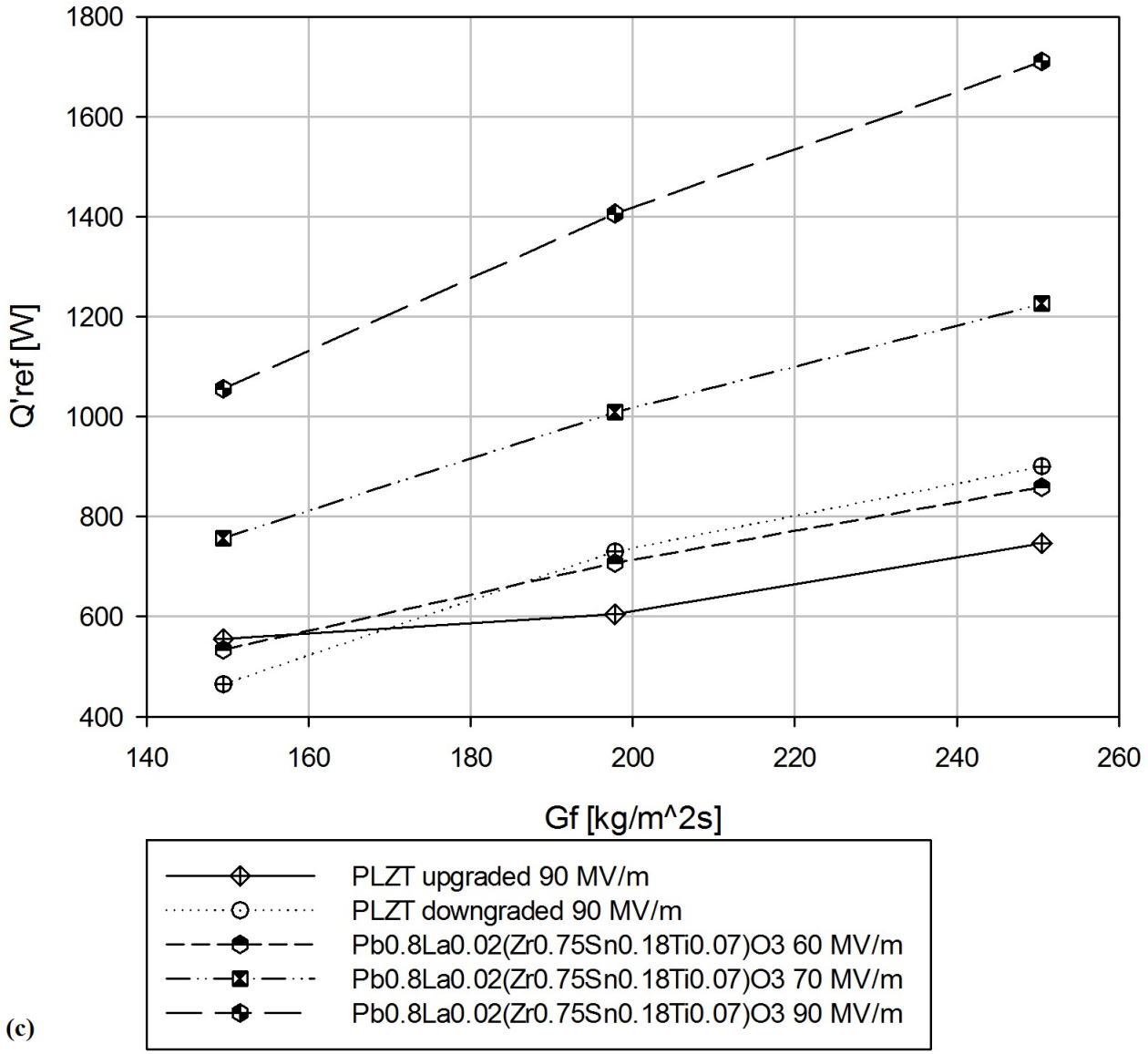
1800
1600
1400
1200
1000
800
600
400
Q'ref [W]
140
160
180
200
220
240
260
Gf [kg/m^2s]
PLZT upgraded 90 MV/m
PLZT downgraded 90 MV/m
Pb0.8La0.02(Zr0.75Sn0.18Ti0.07)O3 60 MV/m
Pb0.8La0.02(Zr0.75Sn0.18Ti0.07)O3 70 MV/m
Pb0.8La0.02(Zr0.75Sn0.18Ti0.07)O3 90 MV/m

(c)

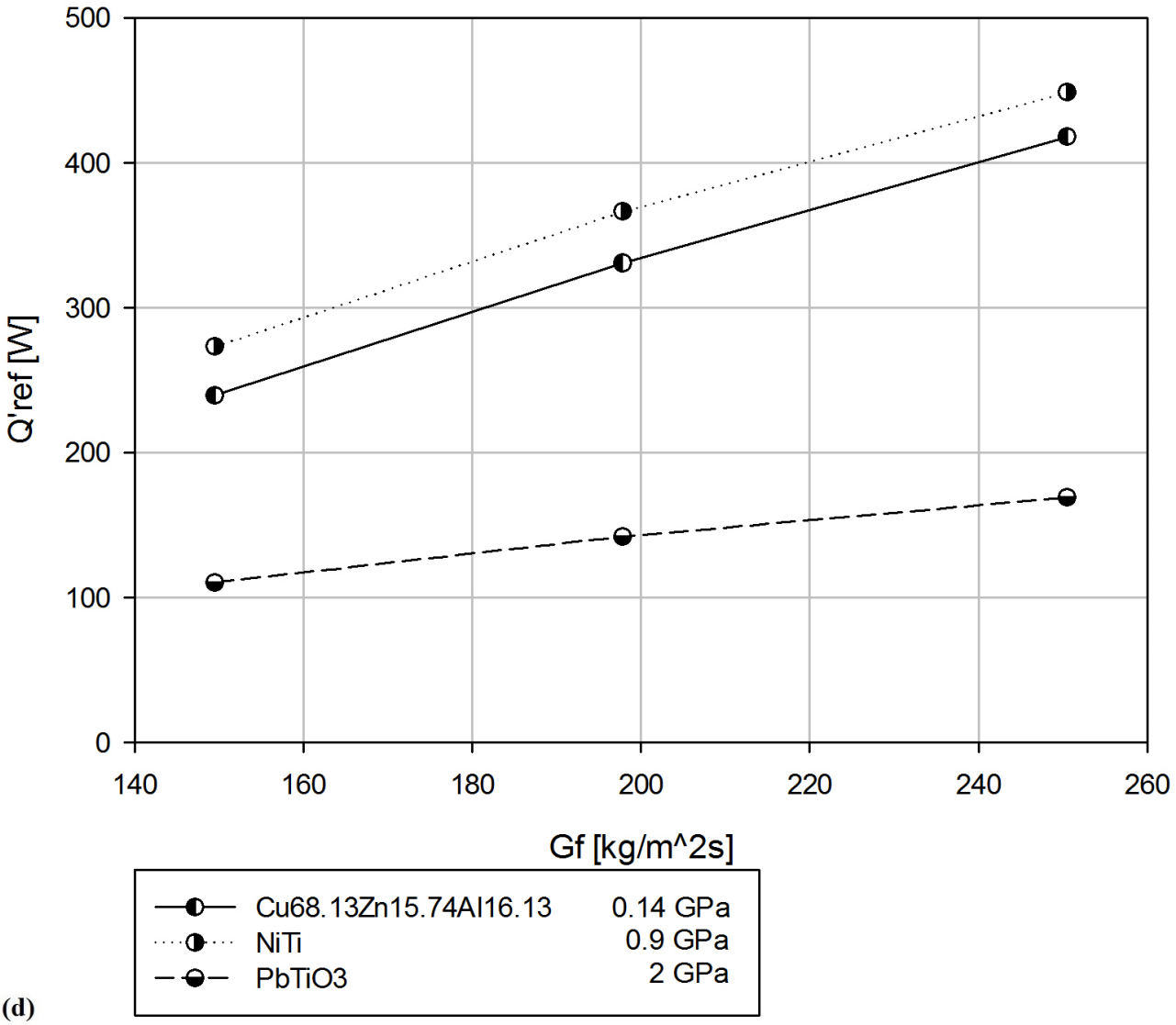
500
400
300
200
100
0
Q'ref [W]
140
160
180
200
220
240
260
Gf [kg/m^2s]
Cu68.13Zn15.74Al16.13
NiTi
PbTiO3
0.14 GPa
0.9 GPa
2 GPa

(d)

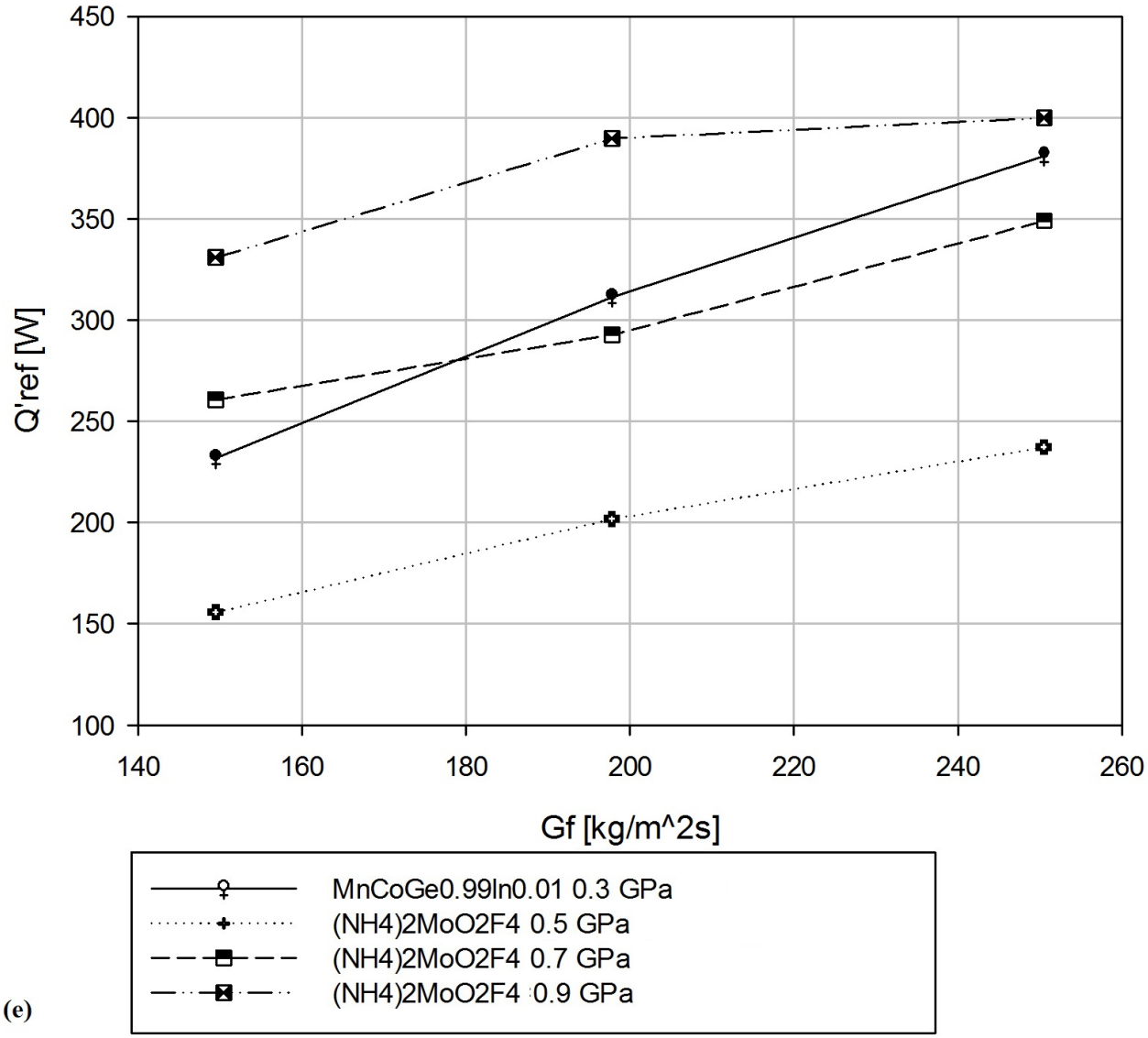

(e)

Figure 11. $\dot{Q}_{ref}$ vs mass flux for: (a) magnetocaloric materials under a magnetic field variation ΔB in [0; 1.5] T; (b) the first and (c) the second group of electrocaloric materials; (d) elastocaloric materials; (e) barocaloric materials.

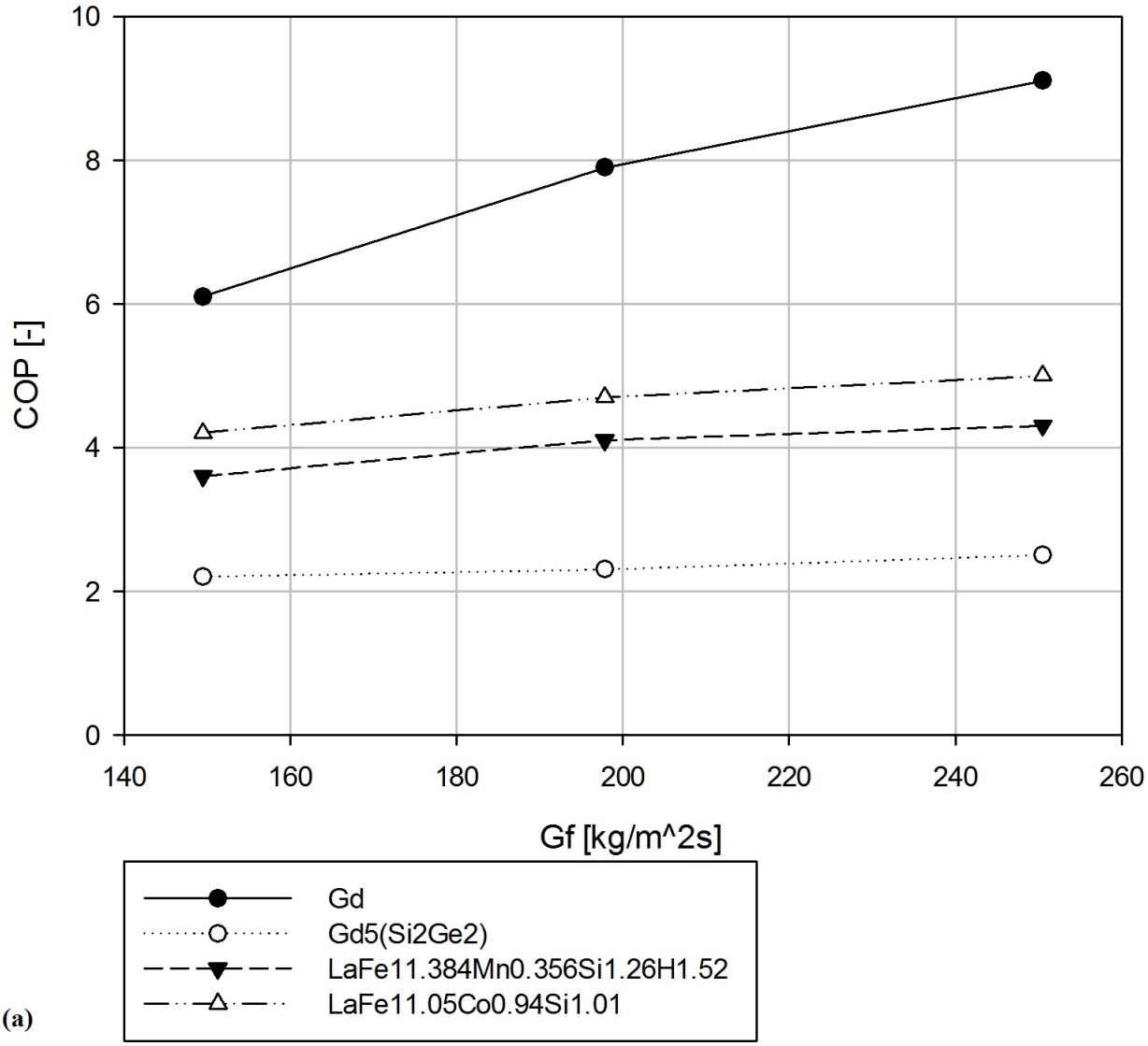
10
8
6
4
2
0
COP [-]
140
160
180
200
220
240
260
Gf [kg/m^2s]
Gd
Gd5(Si2Ge2)
LaFe11.384Mn0.356Si1.26H1.52
LaFe11.05Co0.94Si1.01

(a)

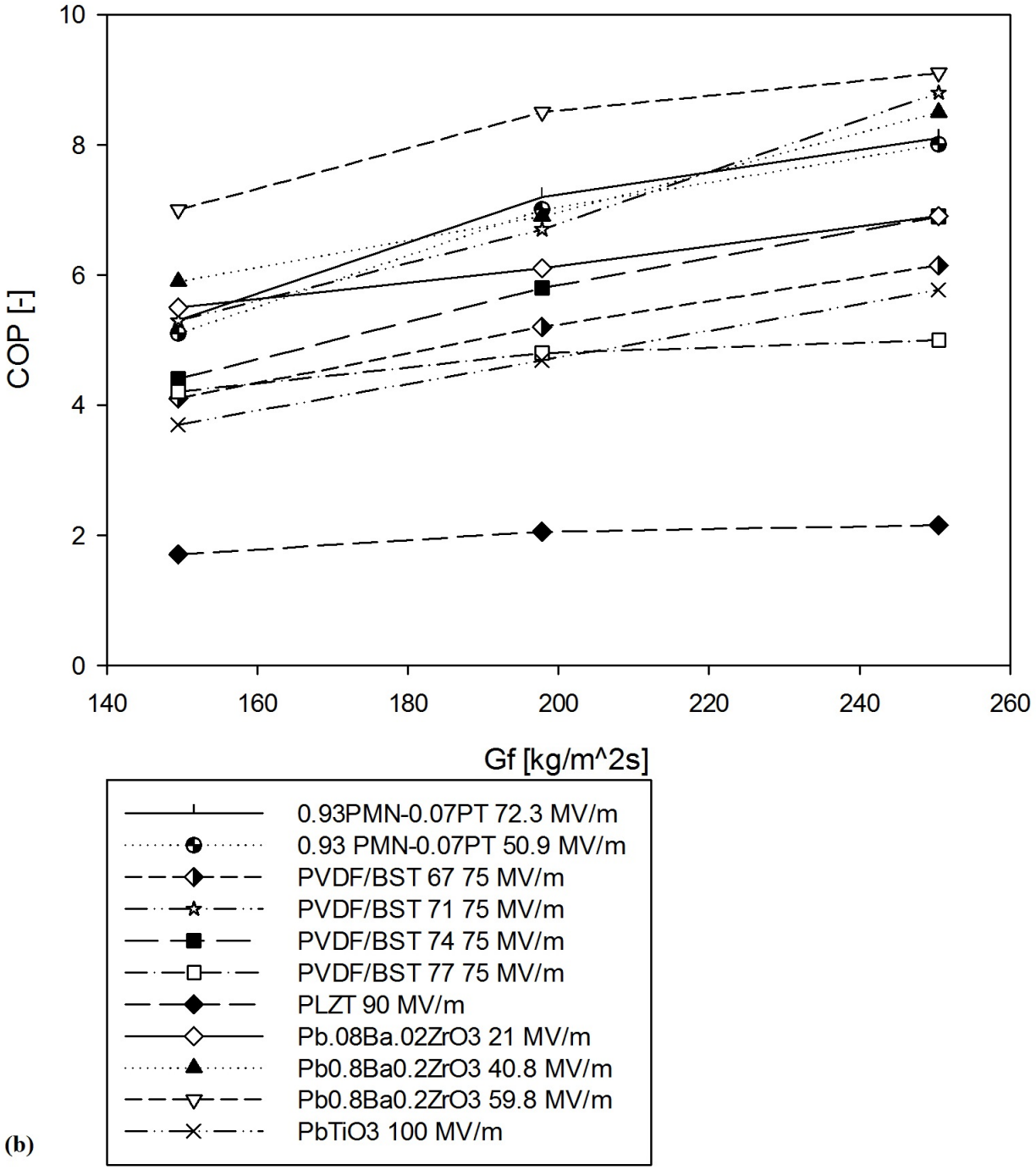
10
8
6
4
2
0
COP [-]
140
160
180
200
220
240
260
Gf [kg/m^2s]
0.93PMN-0.07PT 72.3 MV/m
0.93 PMN-0.07PT 50.9 MV/m
PVDF/BST 67 75 MV/m
PVDF/BST 71 75 MV/m
PVDF/BST 74 75 MV/m
PVDF/BST 77 75 MV/m
PLZT 90 MV/m
Pb.08Ba.02ZrO3 21 MV/m
Pb0.8Ba0.2ZrO3 40.8 MV/m
Pb0.8Ba0.2ZrO3 59.8 MV/m
PbTiO3 100 MV/m

(b)

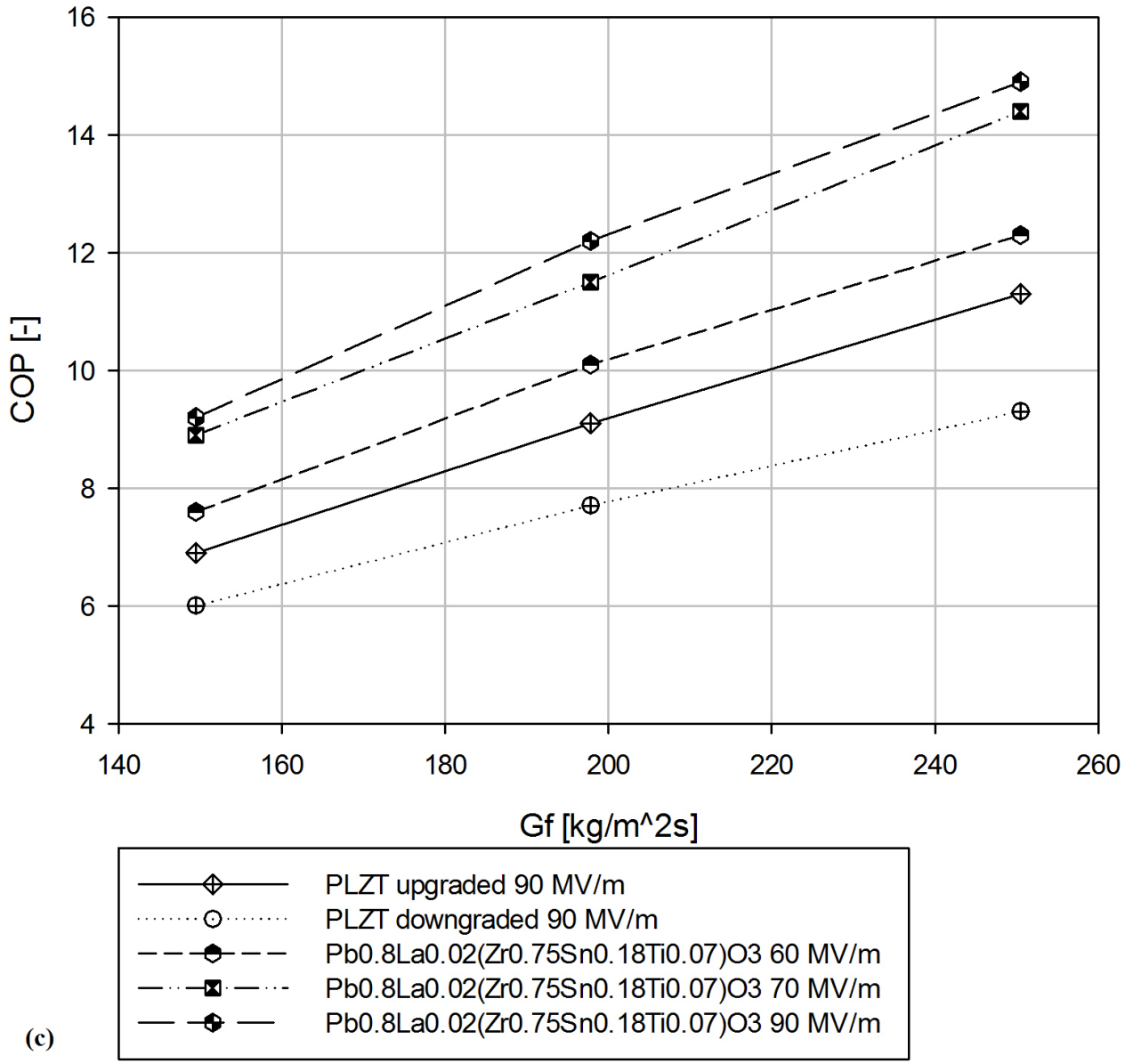
16
14
12
10
8
6
4
COP [-]
140
160
180
200
220
240
260
Gf [kg/m^2s]
PLZT upgraded 90 MV/m
PLZT downgraded 90 MV/m
Pb0.8La0.02(Zr0.75Sn0.18Ti0.07)O3 60 MV/m
Pb0.8La0.02(Zr0.75Sn0.18Ti0.07)O3 70 MV/m
Pb0.8La0.02(Zr0.75Sn0.18Ti0.07)O3 90 MV/m

(c)

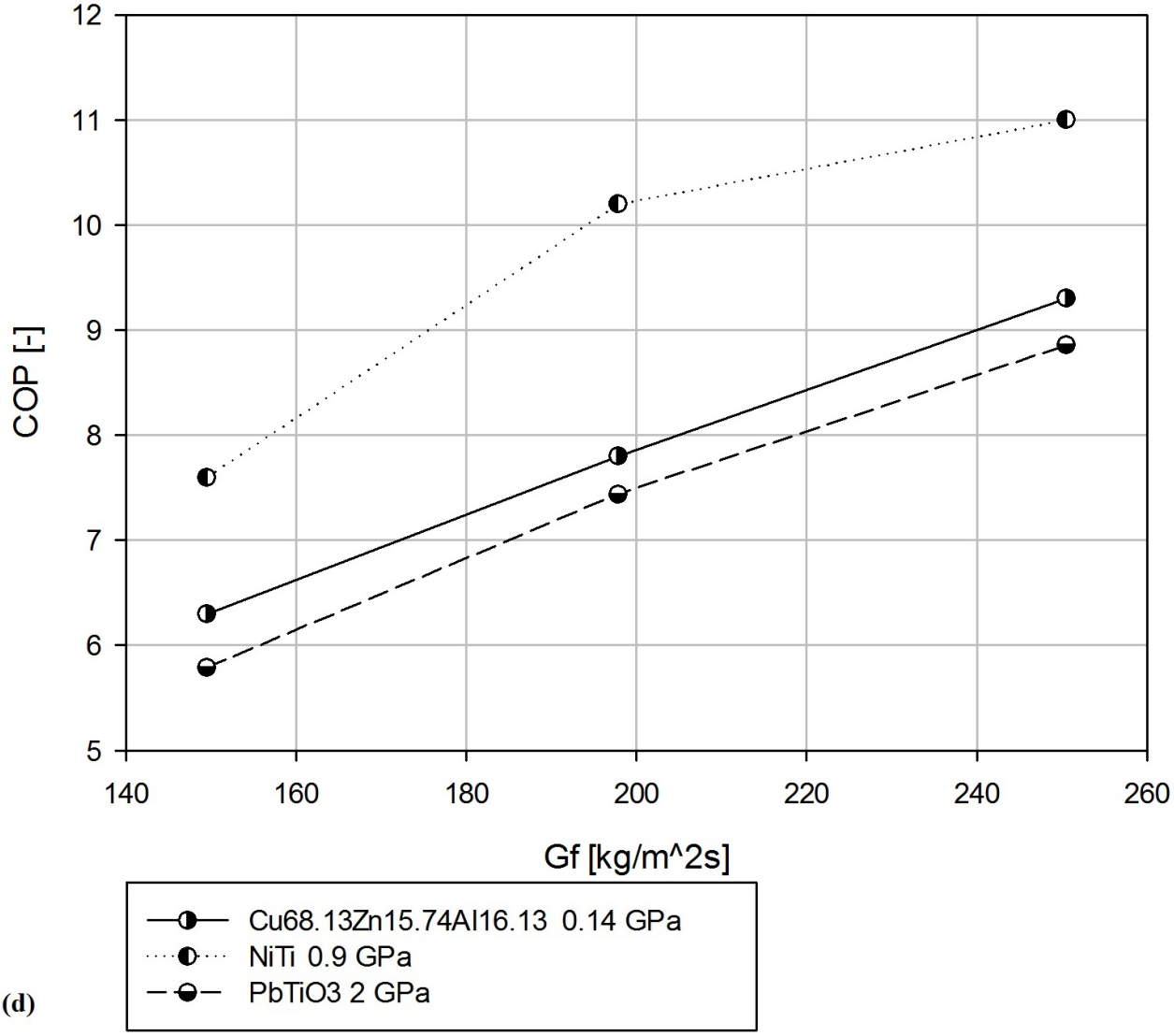
12
11
10
9
8
7
6
5
COP [-]
140
160
180
200
220
240
260
Gf [kg/m^2s]
Cu68.13Zn15.74Al16.13 0.14 GPa
NiTi 0.9 GPa
PbTiO3 2 GPa

(d)

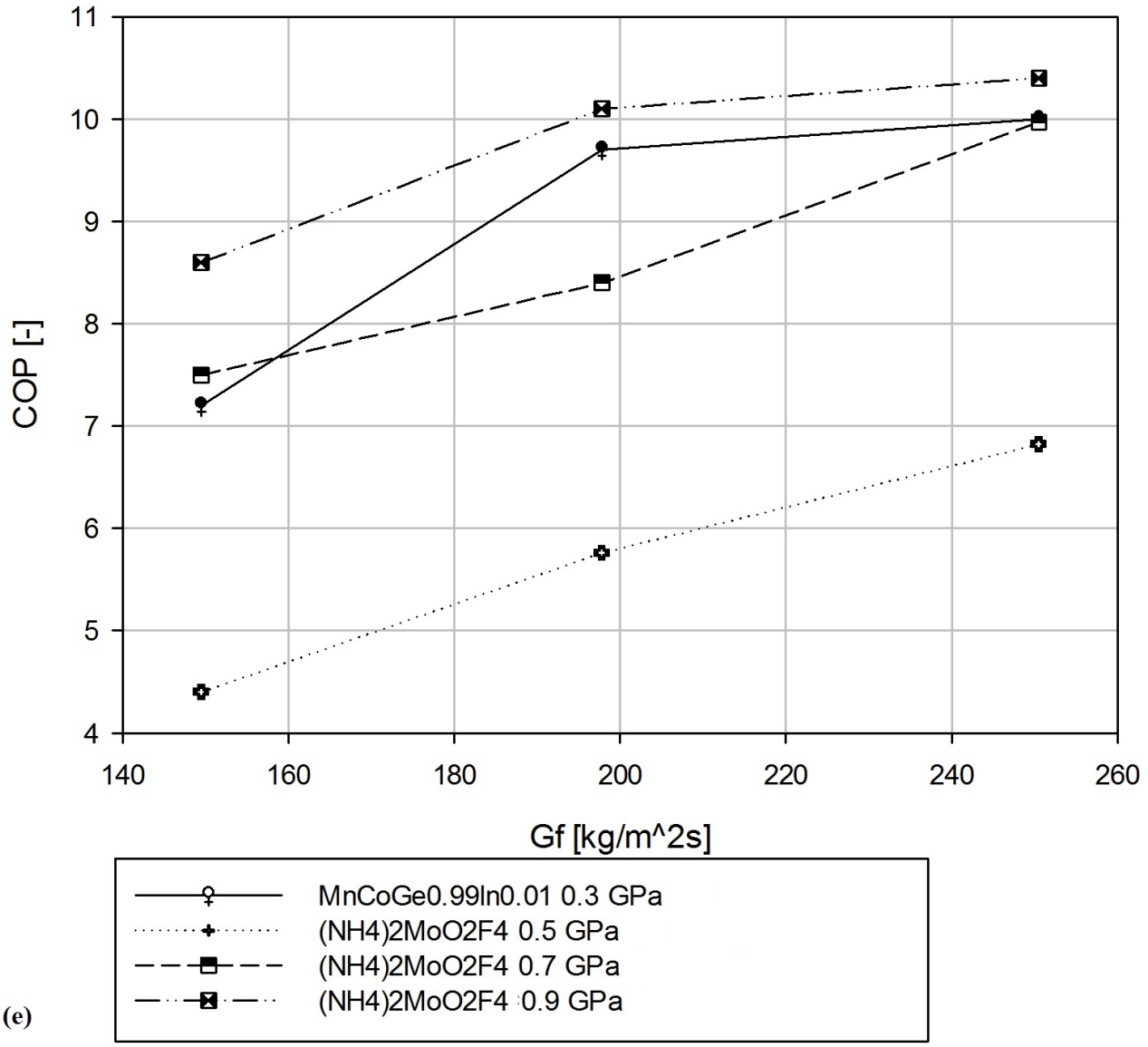

(e)

Figure 12. COP vs mass flux for: (a) magnetocaloric materials under a magnetic field variation ΔB in [0; 1.5] T; (b) the first and (c) the second group of electrocaloric materials; (d) elastocaloric materials; (e) barocaloric materials.

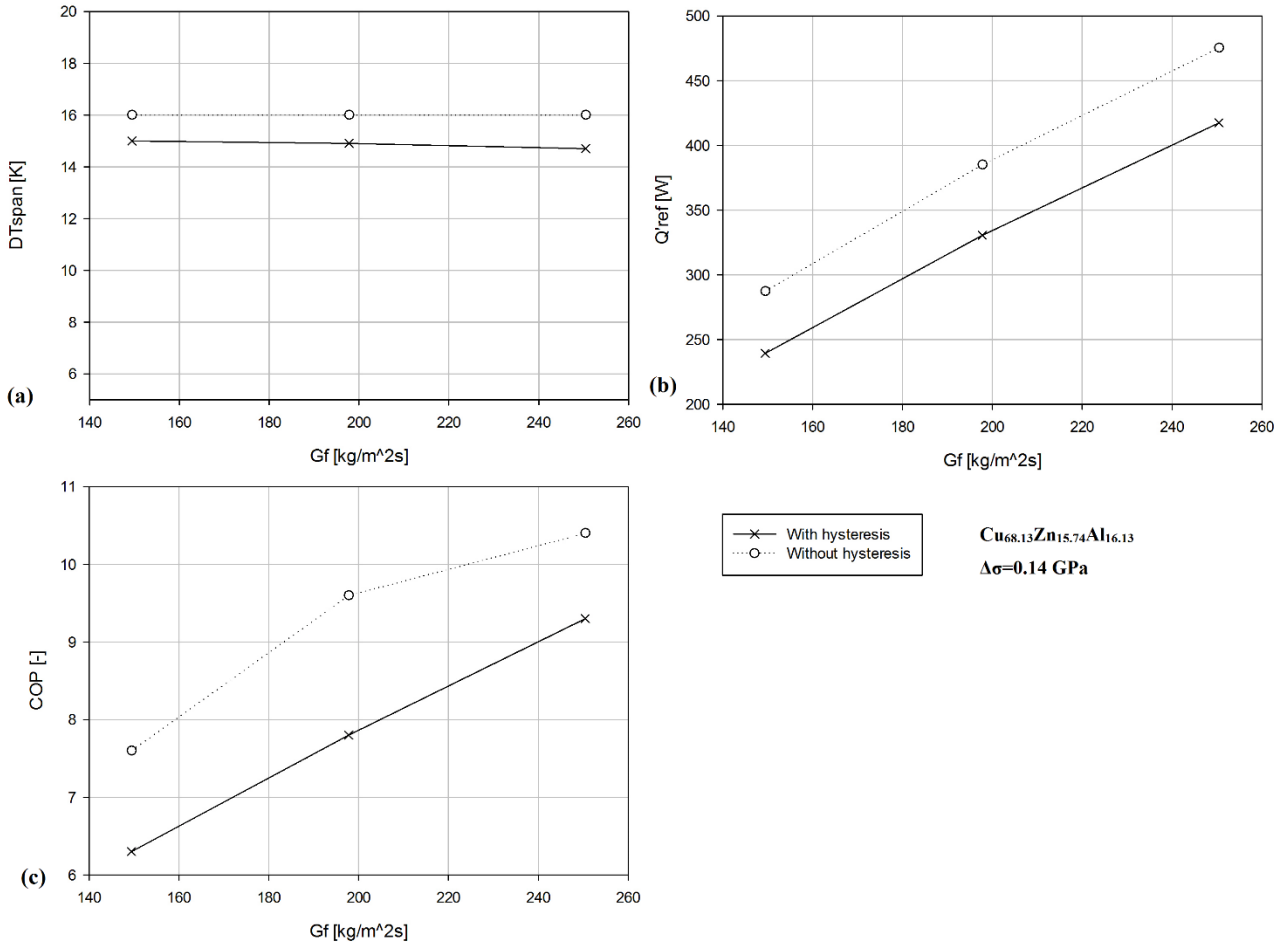

Figure 13. The influence of the hysteresis in the energy performances of $Cu_{68.13}Zn_{15.74}Al_{16.13}$ under an uniaxially driven field change of Δσ=0.14 GPa: (a) ΔT_{span}; (b) $\dot{Q}_{ref}$ and (c) COP vs mass flux.

6. Conclusions

In this paper are reported the energy performances of an Active Caloric Regenerator employing a vast number of solid-state caloric candidates. The investigation has been conducted by means of a 2D numerical model whose peculiarity is the possibility to employ refrigerants regardless to the specific nature of the caloric effect. Temperature span, cooling power and coefficient of performance are the indexes through which the comparison is carried out. The tests are performed at a fixed AMR cycle frequency (1.25 Hz), in the temperature range 292 – 300 K, varying the mass flux in the range 150 - 250 kg $s^{-1}m^{-2}$. The most promising caloric materials that have been tested as refrigerants are: Gd, $Gd_5Si_2Ge_2$, $LaFe_{11.384}Mn_{0.356}Si_{1.26}H_{1.52}$, $LaFe_{11.05}$ $Co_{0.94}Si_{1.10}$ (MMs); P(VDF-TrFE-CFE)/BST polymers, 0.93PMN-0.07PT thin film, the Pb_{1-3x}/2LaxZr$_{0.85}$Ti$_{0.15}$O$_3$ with single and variable compositions, $PbTiO_3$, $Pb_{0.8}Ba_{0.2}ZrO_3$, $Pb_{0.97}La_{0.02}(Zr_{0.75}Sn_{0.18}Ti_{0.07})O_3$(ECMs); $Cu_{68.13}Zn_{15.74}Al_{16.13}$, NiTi, $PbTiO_3$ (eCMs); $(NH_4)_2MoO_2F_4$, $MnCoGe_{0.99}In_{0.01}$ (BCMs). From the simulations the following conclusions can be drawn:

(1) due mostly to the limited magnetic field obtainable by permanent magnets, MMs show the worst performance compared to all the other caloric materials. ΔT_{span} never exceed 10.5 K with a cooling power lower than 128W. Thus, they can be used only for small-scale refrigeration and for a limited number of applications. Within the MMs, the benchmark material of this technology (Gd) show the best performances. Gd belongs to the family of rare earth and therefore is a very expensive material.

(2) ECMs materials show better performances. In particular the PLZT class: $Pb_{1-3x/2}La_xZr_{0.85}Ti_{0.15}O_3$ (in variable composition) and $Pb_{0.97}La_{0.02}(Zr_{0.75}Sn_{0.18}Ti_{0.07})O_3$ overperform the other caloric materials. The best performance can be obtained with $Pb_{0.97}La_{0.02}(Zr_{0.75}Sn_{0.18}Ti_{0.07})O_3$ that ensures ΔT_{span} greater than 40K, with a cooling load between 1010 W and 1800 W. Therefore, an electrocaloric refrigerator working with $Pb_{0.97}La_{0.02}(Zr_{0.75}Sn_{0.18}Ti_{0.07})O_3$ can be applied for a broader scope of commercial applications.

(3) In the class of mechanocaloric cooling (eCMs and BCMs) the performances are comparable. The best material of this class is NiTi, with a ΔT_{span} of 15K and cooling loads between 280 and 460 W.

(4) Due to the different weight of the work associated with the variation of the driven field and to the influence of the hysteresis that affects the Giant caloric materials COPs of many first order transition materials are lower that they would be without considering hysteresis as shown as an example for $Cu_{68.13}Zn_{15.74}Al_{16.13}$ with an average percentage decrease of -18%.

(5) The best COP obtained, under our operative conditions and carried out by the introduced numerical investigation, are proper of $Pb_{0.97}La_{0.02}(Zr_{0.75}Sn_{0.18}Ti_{0.07})O_3$ with a maximum value of 15.

Therefore, from the results collected among ECM materials, $Pb_{0.97}La_{0.02}(Zr_{0.75}Sn_{0.18}Ti_{0.07})O_3$ strongly overperforms the other caloric materials. Other advantages carried by the AER cycle are: electric fields very easy to generate; a large variation of the electric field obtainable by simply charging and discharging an EM capacitor; very simpleness in realizing a miniaturized refrigerator based on ECE; the chipness and the availabilitness of the EM materials; the wide range of temperature in which EM materials can work; an AER operates with little or no vibrations and with no moving parts; an AER cycle can work with energy recovery because of the unused electrical work may be easily recovered for subsequent cycles using an electronic circuitry. In conclusion, downstream of this investigation and with reference to the working condition imposed, electrocaloric refrigeration globally confers the most promising results. Anyhow the way to award it the title of “environmentally friendly technology of the future” is still long. Further studies, investigations and tests must be performed, under an extensive set of different operative conditions in order to observe such technique under many different situations.

REFERENCES

[1] S.Choi, U. Han, H. Cho, H. Lee. Review: Recent advances in household refrigerator cycle technologies. Applied Thermal Engineering. 132 560–574 (2018).

[2] *Montreal Protocol on substances that deplete the ozone layer*, United Nation Environment Program (UN), New York, NY, USA, 1987.

[3] *Kyoto Protocol to the United Nation Framework Convention on Climate Change,* United Nation Environment Program (UN), Kyoto, JPN, 1997.
[4] C. Aprea, A. Greco, A. Maiorino, C. Masselli. The drop-in of HFC134a with HFO1234ze in a household refrigerator, International Journal of Thermal Sciences 127, 117-125 (2018).
[5] A. Kitanovski, U. Plaznik, U. Tomc, A. Poredoš. Present and future caloric refrigeration and heat-pump technologies. International Journal of Refrigeration, 57, 288-298 (2015).
[6] S. Qian, D. Nasuta, A. Rhoads, Y. Wang, Y. Geng, Y. Hwang, R. Radermacher, I. Takeuchi. Not-in-kind cooling technologies: A quantitative comparison of refrigerants and system performance. international journal of refrigeration, 62, 177-192 (2016).
[7] X. Moya, E. Defay, V. Heine, N. D. Mathur. Too cool to work. Nature Physics, 11(3), 202 (2015).
[8] P. Weiss and A. Piccard. Sur un nouveau phénomène magnétocalorique. Comptes Rendus, 166, pp.352-354 (1918).
[9] J.A. Barclay. The theory of an active magnetic regenerative refrigerator. NASA STI/Recon Technical Report N 83, 34087 (1982).
[10] J. R. Hull, K. L. Uherka. Magnetic heat pumps for near-room-temperature applications. Energy, Volume 14 (4), 177-185 (1989).
[11] A. Kitanovski, J. Tusek, U. Tomc, U. Plaznik, M. Ozbolt, A. Poredos. Overview of existing magnetocaloric prototype devices. In: Magnetocaloric Energy Conversion. Springer International Publishing, 269–330 (2015).
[12] Y. Kotani, Y. Kansha, A. Tsutsumi. Conceptual design of an active magnetic regenerative heat circulator based on self-heat recuperation technology. Energy, 55, 127-133 (2013).
[13] C. Aprea, G. Cardillo, A. Greco, A. Maiorino, C. Masselli, A rotary permanent magnet magnetic refrigerator based on AMR cycle, Applied Thermal Engineering, 101 699-703 (2016).
[14] D. J. Silva, B. D. Bordalo, A. M. Pereira, J. Ventura, J. P. Araújo. Solid state magnetic refrigerator. Applied Energy, 93, 570-574 (2012).
[15] J. A. Lozano, K. Engelbrecht, C. R. Bahl, K. K. Nielsen, D. Eriksen, U. L. Olsen, J.R. Barbosa, A. Smith, A.T. Prata, N. Pryds. Performance analysis of a rotary active magnetic refrigerator. Applied Energy, 111, 669-680 (2013).
[16] A. Kitanovski, P.W. Egolf, Innovative ideas for future research on magnetocaloric technologies, International Journal of Refrigeration, 33 449-464 (2010).
[17] P. V. Trevizoli, G. F. Peixer, A. T. Nakashima, M. S. Capovilla, J. A. Lozano, J. R Barbosa Jr. Influence of inlet flow maldistribution and carryover losses on the performance of thermal regenerators. Applied Thermal Engineering, 133, 472-482 (2018).
[18] P. V. Trevizoli, A. T. Nakashima, G. F. Peixer, J. R. Barbosa Jr. Performance assessment of different porous matrix geometries for active magnetic regenerators. Applied Energy, 187, 847-861 (2017).
[19] R. Teyber, P. V. Trevizoli, T. V. Christiaanse, P. Govindappa, P. Niknia, A. Rowe. Semi-analytic AMR element model. Applied Thermal Engineering, 128, 1022-1029 (2018).
[20] D. J. Silva, J. Ventura, J. P. Araújo, A. M. Pereira. Maximizing the temperature span of a solid state active magnetic regenerative refrigerator. Applied Energy, 113, 1149-1154 (2014).
[21] J. M. D. Coey. Permanent magnets: Plugging the gap. Scripta Materialia, 67(6), 524-529 (2012).
[22] M. Ožbolt, A. Kitanovski, J. Tušek, A. Poredoš. Electrocaloric refrigeration: thermodynamics, state of the art and future perspectives. International journal of refrigeration, 40, 174-188 (2014).
[23] O.V. Pakhomov, S.F. Karmaneko, A.A. Semenov, A.S. Starkov, A.V. Es'kov. Thermodynamic estimation of cooling efficiency using an electrocaloric solid-state line. Tech. Phys. 55 (8), 1155–1160 (2010).
[24] M. Valant. Electrocaloric materials for future solid-state refrigeration technologies. Progress in Materials Science, 57(6), 980-1009 (2012).
[25] J. F. Scott. Electrocaloric materials. Annual Review of Materials Research, 41, 229-240 (2011).
[26] H. Gu, X. Qian, X. Li, B. Craven, W. Zhu, A. Cheng, S. C. Yao[4], Q. M. Zhang. A chip scale electrocaloric effect based cooling device. Applied Physics Letters, 102(12), 122904 (2013).
[27] Y. D. Wang, S. J. Smullin, M. J. Sheridan, Q. Wang, C. Eldershaw, D.E. Schwartz. A heat-switch-based electrocaloric cooler. Applied Physics Letters, 107(13), 134103 (2015).
[28] J. Tušek, K. Engelbrecht, R. Millán-Solsona, L. Mañosa, E. Vives, L.P. Mikkelsen, N. Pryds. The elastocaloric effect: a way to cool efficiently. Advanced Energy Materials, 5(13) (2015).
[29] T. Strässle, A. Furrer, K. A. Müller. Cooling by adiabatic application of pressure–the barocaloric effect. Physica B: Condensed Matter, 276, 944-945 (2000).

[30] L. Mañosa, A. Planes, M. Acet. Advanced materials for solid-state refrigeration. Journal of Materials Chemistry A, 1 (16), 4925-4936 (2013).
[31] B. Lu, J. Liu. Mechanocaloric materials for solid-state cooling. Science bulletin, 60(19), 1638-1643 (2015).
[32] S. Qian, Y. Geng, Y. Wang, J. Ling, Y. Hwang, R. Radermacher, I. Takeuchi, J. Cui. A review of elastocaloric cooling: materials, cycles and system integrations. International Journal of Refrigeration, 64, 1-19 (2016).
[33] J. M. Bermúdez-García, M. Sánchez-Andújar, M. A. Señarís-Rodríguez. A New Playground for Organic–Inorganic Hybrids: Barocaloric Materials for Pressure-Induced Solid-State Cooling, J. Phys. Chem. Lett., 8 (18), 4419–4423 (2017).
[34] J. Tušek, K. Engelbrecht, D. Eriksen, S. Dall'Olio, J. Tušek, N. Pryds. A regenerative elastocaloric heat pump. Nature Energy, 1(10), 16134 (2016).
[35] D. Luo, Y. Feng, P. Verma. Modeling and analysis of an integrated solid state elastocaloric heat pumping system. Energy, 130, 500-514 (2017).
[36] H. Ossmer, F. Wendler, M. Gueltig, F. Lambrecht, S. Miyazaki, M. Kohl. Energy-efficient miniature-scale heat pumping based on shape memory alloys. Smart Materials and Structures, 25(8), 085037 (2016).
[37] K. Engelbrecht, J. Tušek, D. Eriksen, T. Lei, C.Y. Lee, J. Tušek, N. Pryds. A regenerative elastocaloric device: experimental results. Journal of Physics D: Applied Physics, 50(42), 424006 (2017).
[38] S. M. Kirsch, M. Schmidt, F. Welsch, N. Michaelis, A. Schütze, S. Seelecke. Development of a shape-memory based air conditioning system. In Engineering for a Changing World: Proceedings; 59th IWK, Ilmenau Scientific Colloquium, Technische Universität Ilmenau, September 11-15, 2017 (Vol. 59, No. 3.1. 03).
[39] K. K. Nielsen, J. Tusek, K. Engelbrecht, S. Schopfer, A. Kitanovski, C. R. H. Bahl, A. Smith, N. Pryds, A. Poredos. Review on numerical modeling of active magnetic regenerators for room temperature applications. International Journal of Refrigeration, 34(3), 603-616 (2011).
[40] C. Aprea, A. Greco, A. Maiorino. Modelling an active magnetic refrigeration system: a comparison with different models of incompressible flow through a packed bed. Applied Thermal Engineering, 36, 296-306 (2012).
[41] C. Aprea, A. Greco, A. Maiorino, C. Masselli. A comparison between rare earth and transition metals working as magnetic materials in an AMR refrigerator in the room temperature range, Appl. Thermal Eng., vol. 91, pp. 767-777 (2015).
[42] V. Franco, J. S. Blázquez, B. Ingale, A. Conde. The magnetocaloric effect and magnetic refrigeration near room temperature: materials and models. Annual Review of Materials Research, 42 (2012).
[43] C. Aprea, A. Maiorino. A flexible numerical model to study an active magnetic refrigerator for near room temperature applications. Applied Energy, 87(8), 2690-2698 (2010).
[44] C. Aprea, A Greco, A. Maiorino, C. Masselli, A comparison between different materials in an active electrocaloric regenerative cycle with a 2D numerical model, International Journal of Refrigeration, vol. 69, pp. 369-382 (2016).
[45] M. Ožbolt, A. Kitanovski, J. Tušek, A. Poredoš. Electrocaloric vs. magnetocaloric energy conversion. International Journal of Refrigeration, 37, 16-27 (2014).
[46] C. Aprea, A. Greco, A. Maiorino, C. Masselli, A comparison between electrocaloric and magnetocaloric materials for solid state refrigeration, International Journal of Heat and Technology, 35 (1), pp. 225-234 (2017).
[47] S. Qian, J. Ling, Y. Hwang, R. Radermacher, I. Takeuchi. Thermodynamics cycle analysis and numerical modeling of thermoelastic cooling systems. International Journal of Refrigeration, 56, 65-80 (2015).
[48] Z. Xie, G. Sebald, D. Guyomar. Comparison of elastocaloric effect of natural rubber with other caloric effects on different-scale cooling application cases. Applied Thermal Engineering, 111, 914-926 (2017).
[49] C. Aprea, A. Greco, A. Maiorino, C. Masselli. A two-dimensional model of a solid-state regenerator based on combined electrocaloric-elastocaloric effect, Energy Procedia, vol. 126, 337–344 (2017).
[50] S. Qian, L. Yuan, J. Yu, G. Yan. Numerical modeling of an active elastocaloric regenerator refrigerator with phase transformation kinetics and the matching principle for materials selection. Energy, 141, 744-756 (2017).

[51] K. A. Gschneidner Jr, V. K. Pecharsky. Magnetocaloric materials. Annual Review of Materials Science, 30(1), 387-429 (2000).
[52] S.Y. Dan'kov, A.M. Tishin, V. K. Pecharsky, K.A. Gschneidner Jr. Magnetic phase transitions and the magneto-thermal properties of gadolinium. Phys Rev. B, vol. 57 (6), pp. 3478-3490 (1998).
[53] A. Waske, H. Hermann, N. Mattern, K. Skokov, O. Gutfleisch, J. Eckert. Magnetocaloric effect of an Fe-based metallic glass compared to benchmark gadolinium. Journal of Applied Physics, 112 (12), 123918 (2012).
[54] V. K. Pecharsky, K. A. Gschneidner Jr. Tunable magnetic regenerator alloys with a giant magnetocaloric effect for magnetic refrigeration from∼ 20 to∼ 290 K. Applied Physics Letters, *70* (24), 3299-3301 (1997).
[55] V. K. Pecharsky, K. A. Gschneidner Jr. Giant magnetocaloric effect in Gd 5 (Si 2 Ge 2). Physical review letters, 78(23), 4494 (1997).
[56] K. Morrison, K.G. Sandeman, L.F. Cohen, C.P. Sasso, V. Basso, A. Barcza, M. Katter, J.D. Moore, K.P. Skokov, O. Gutfleisch. Evaluation of the reliability of the measurement of key magnetocaloric properties: a round robin study of La(Fe,Si,Mn)Hδ conducted by the SSEEC consortium of European laboratories. *Int. J. Refr.*, 35 (6), 1528-1536 (2012).
[57] R. Bjørk, C.R.H. Bahl, M. Katter. Magnetocaloric properties of LaFe13-x-yCoxSiy and commercial grade Gd. *J. Magn. Magn. Mater.*, vol. 322 (24), pp. 3882-3888 (2010).
[58] S. Fujieda, A. Fujita, K. Fukamichi. Large magnetocaloric effects in NaZn13-type La (FexSi1− x) 13 compounds and their hydrides composed of icosahedral clusters. Science and Technology of Advanced Materials, 4(4), 339-346 (2003).
[59] M. Valant. Electrocaloric materials for future solid-state refrigeration technologies. Progress in Materials Science, 57(6), 980-1009 (2012).
[60] S. G. Lu, Q. Zhang. Electrocaloric materials for solid-state refrigeration. Advanced Materials, 21(19), 1983-1987 (2009).
[61] A. Javadi, Y. Xiao, W. Xu, S. Gong. Chemically modified graphene/P (VDF-TrFE-CFE) electroactive polymer nanocomposites with superior electromechanical performance. Journal of Materials Chemistry, 22(3), 830-834 (2012).
[62] G. Zhang, Q. Li, H. Gu, S. Jiang, K. Han, M.R. Gadinski, Q. Wang. Ferroelectric Polymer Nanocomposites for Room-Temperature Electrocaloric Refrigeration. Advanced materials, 27(8), 1450-1454 (2015).
[63] M.A. Hamad. Room temperature giant electrocaloric properties of relaxor ferroelectric 0.93PMN-0.07 PT thin film. AIP Adv. 3, 032115, (2013).
[64] T. M. Correia, J. S. Young, R. W. Whatmore, J. F. Scott, N. D. Mathur, Q. Zhang. Investigation of the electrocaloric effect in a PbMg1/3Nb2/3O3-PbTiO3 relaxor thin film. Applied Physics Letters, 95(18), 182904 (2009).
[65] S. Lisenkov, B. K. Mani, C. M. Chang, J. Almand, I. Ponomareva. Multicaloric effect in ferroelectric PbTiO 3 from first principles. Physical Review B, 87(22), 224101 (2013).
[66] Y. Zhao, X. Hao, Q. Zhang. Energy-storage properties and electrocaloric effect of Pb(1–3x/2)LaxZr0.85Ti0.15O3 antiferroelectric thick films. ACS Appl. Mater. Interfaces 6, 11633–21639 (2014).
[67] Y. Zhao, X. Hao, Q. Zhang. Enhanced energy-storage performance and electrocaloric effect in compositionally graded Pb(1–3x/2)LaxZr0.85Ti0.15O3. Ceram. Int. 42, 1679–1687 (2016).
[68] B. Peng, H. Fan, Q.A. Zhang. A giant electrocaloric effect in nanoscale antiferroelectric and ferroelectric phases coexisting in a relaxor Pb0.8Ba0.2ZrO3 thin film at room temperature. Advanced Functional Materials, vol. 23(23), pp. 2987-2992 (2013).
[69] Y. Zhao, X. Hao, Q. Zhang. A giant electrocaloric effect of a Pb0.97La0.02(Zr0.75Sn0.18Ti0.07)O3 antiferroelectric thick film at room temperature. Journal of Materials Chemistry C, vol. 3(8), pp. 1694-1699 (2015).
[70] C. M. Wayman, K. Ōtsuka. Shape memory materials. Cambridge University Press (1998).
[71] Bonnot, E., Romero, R., Mañosa, L., Vives, E., & Planes, A. Elastocaloric effect associated with the martensitic transition in shape-memory alloys. Physical review letters, vol. 100(12), 125901 (2008).
[72] J. Tušek, K. Engelbrecht, R. Millán-Solsona, L. Mañosa, E. Vives, L.P. Mikkelsen, N. Pryds. The elastocaloric effect: a way to cool efficiently. Advanced Energy Materials, vol. 5 (13), (2015).

[73] M. V. Gorev, E. V. Bogdanov, I. N. Flerov, A. G. Kocharova, N. M. Laptash. Investigation of thermal expansion, phase diagrams, and barocaloric effect in the (NH 4) 2 WO 2 F 4 and (NH 4) 2 MoO 2 F 4 oxyfluorides. Physics of the Solid State, vol. 52(1), pp. 167-175 (2010).

[74] R. R. Wu, L. F. Bao, F. X. Hu, H. Wu, Q.Z. Huang, J. Wang, X.L. Dong, G. N. Li, J. R. Sun, F. R. Shen, T. Y. Zhao, X. Q. Zheng, L. C. Wang, Y. Liu, W.L. Zuo, Y. Y., Zhao, M. Zhang, X.C. Wang, C.Q. Jin, G. H. Rao, X. F. Han, B. G. Shen. Giant barocaloric effect in hexagonal Ni 2 In-type Mn-Co-Ge-In compounds around room temperature. Scientific reports, vol. 5, 18027 (2015).

[75] C. Aprea, A. Greco, A. Maiorino, C. Masselli. Energy performances and numerical investigation of solid-state magnetocaloric materials used as refrigerant in an active magnetic regenerator. Thermal Science and Engineering Progress, vol. 6, pp. 370-379 (2018).

[76] Brey, W., Nellis, G., & Klein, S. Thermodynamic modeling of magnetic hysteresis in AMRR cycles. International Journal of Refrigeration, vol. 47, pp. 85-97, (2014).